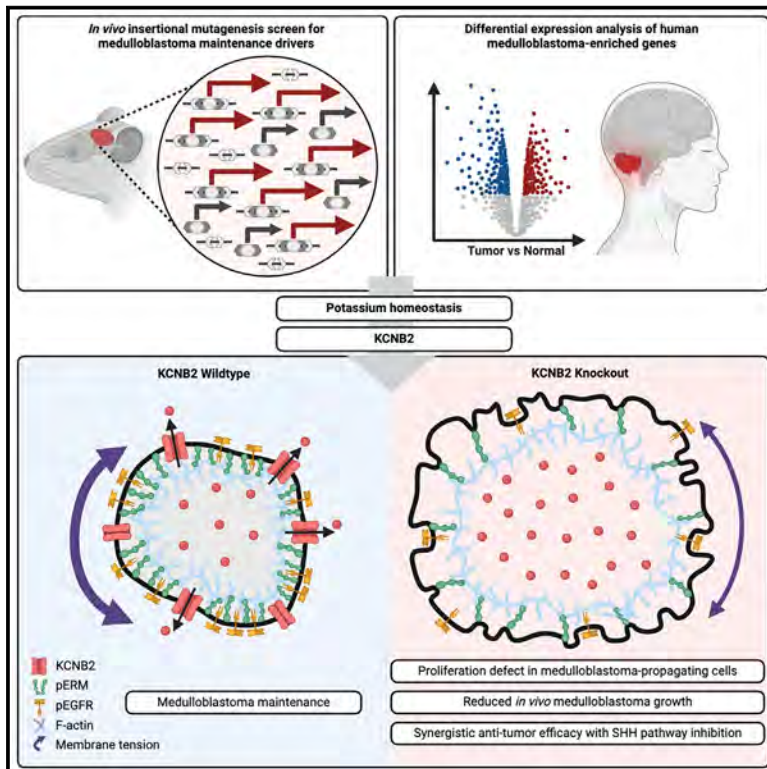


Developmental Cell

A forward genetic screen identifies potassium channel essentiality in SHH medulloblastoma maintenance

Graphical abstract



Authors

Jerry J. Fan, Anders W. Erickson, Julia Carrillo-Garcia, ..., Yu Sun, Michael D. Taylor, Xi Huang

Correspondence

mdt.cns@gmail.com (M.D.T.), xi.huang@sickkids.ca (X.H.)

In brief

Fan et al. develop a double-jumping transposon to identify cancer maintenance drivers through *in vivo* functional genomics. The screen identifies potassium channel KCNB2 as a maintenance driver that orchestrates potassium homeostasis, plasma membrane tension, and biochemical signaling to promote medulloblastoma growth.

Highlights

- Lazy Piggy transposon enables *in vivo* screening for cancer maintenance drivers
- Lazy Piggy screens implicate potassium homeostasis in medulloblastoma maintenance
- KCNB2 drives medulloblastoma by controlling biomechanical and biochemical signaling
- KCNB2 depletion synergizes with targeted therapy to enhance anti-tumor efficacy

Article

A forward genetic screen identifies potassium channel essentiality in SHH medulloblastoma maintenance

Jerry J. Fan,^{1,2,3,28} Anders W. Erickson,^{1,2,28} Julia Carrillo-Garcia,^{1,2,28} Xin Wang,^{1,2,28} Patryk Skowron,^{1,2,28} Xian Wang,^{1,2,4} Xin Chen,^{1,2,5} Guanqiao Shan,⁴ Wenkun Dou,⁴ Shahrzad Bahrapour,^{1,2} Yi Xiong,^{1,2,6,7} Weifan Dong,^{1,2,3} Namal Abeyundara,^{1,2} Michelle A. Francisco,^{1,2} Ronwell J. Pusong,^{1,2} Wei Wang,^{1,2} Miranda Li,^{1,2} Elliot Ying,^{1,2} Raúl A. Suárez,^{1,2} Hamza Farooq,^{1,2,8} Borja L. Holgado,^{1,2} Xiaochong Wu,^{1,2,23,24} Craig Daniels,^{1,2,23,24} Adam J. Dupuy,⁹ Juan Cadiñanos,¹⁰ Allan Bradley,¹¹ Anindya Bagchi,¹² Branden S. Moriarity,¹³ David A. Largaespada,¹³ A. Sorana Morrissy,^{1,2,14,15,16} Vijay Ramaswamy,^{1,2,17} Stephen C. Mack,^{1,2,18} Livia Garzia,^{1,2,19,20} Peter B. Dirks,^{1,2,3,21} Xuejun Li,^{6,7} Siyi Wanggou,^{1,2,6,7} Sean Egan,^{2,3,22} Yu Sun,⁴ Michael D. Taylor,^{1,2,8,21,23,24,25,26,27,*} and Xi Huang^{1,2,3,29,*}

¹Developmental and Stem Cell Biology Program, The Hospital for Sick Children, Toronto, ON M5G 0A4, Canada

²Arthur and Sonia Labatt Brain Tumour Research Centre, The Hospital for Sick Children, Toronto, ON M5G 0A4, Canada

³Department of Molecular Genetics, University of Toronto, Toronto, ON M5S 1A8, Canada

⁴Department of Mechanical and Industrial Engineering, University of Toronto, Toronto, ON M5S 3E1, Canada

⁵Songjiang Research Institute, Shanghai Key Laboratory of Emotions and Affective Disorders, Songjiang Hospital Affiliated to Shanghai Jiao Tong University School of Medicine, Shanghai 200032, China

⁶Department of Neurosurgery, Xiangya Hospital, Central South University, Changsha, Hunan 410008, China

⁷Hunan International Scientific and Technological Cooperation Base of Brain Tumor Research, Xiangya Hospital, Central South University, Changsha, Hunan 410008, China

⁸Department of Laboratory Medicine and Pathobiology, University of Toronto, Toronto, ON M5S 3E1, Canada

⁹Department of Anatomy & Cell Biology, Carver College of Medicine, University of Iowa, Iowa City, IA 52246, USA

¹⁰Instituto de Medicina Oncológica y Molecular de Asturias (IMOMA), Oviedo 33193, Spain

¹¹T-Therapeutics Ltd. One Riverside, Granta Park, Cambridge CB21 6AD, UK

¹²Tumor Initiation and Maintenance Program, Sanford Burnham Prebys Medical Discovery Institute, La Jolla, CA 92037, USA

¹³Masonic Cancer Center, Department of Pediatrics, and Center for Genome Engineering, University of Minnesota, Minneapolis, MN 55455, USA

¹⁴Arnie Charbonneau Cancer Institute, University of Calgary, Calgary, AB T2N 4Z6, Canada

¹⁵Alberta Children's Hospital Research Institute, University of Calgary, Calgary, AB T2N 4N1, Canada

¹⁶Department of Biochemistry and Molecular Biology, Cumming School of Medicine, University of Calgary, Calgary, AB T2N 2T8, Canada

¹⁷Department of Paediatrics, University of Toronto, Toronto, ON M5G 1X8, Canada

¹⁸Department of Developmental Neurobiology, Neurobiology and Brain Tumor Program, Center of Excellence in Neuro-Oncology Sciences, St Jude Children's Hospital, Memphis, TN 38105, USA

¹⁹Department of Surgery, Division of Orthopedic Surgery, McGill University, Montreal, QC H4A 3J1, Canada

²⁰Cancer Research Program, RI-MUHC, Montreal, QC H4A 3J1, Canada

²¹Department of Surgery, University of Toronto, Toronto, ON M5S 1A8, Canada

²²Cell Biology Program, The Hospital for Sick Children, Toronto, ON M5G 0A4, Canada

²³Texas Children's Cancer and Hematology Center, Houston, TX 77030, USA

²⁴Department of Pediatrics, Hematology/Oncology, Baylor College of Medicine, Houston, TX 77030, USA

²⁵Department of Neurosurgery, Baylor College of Medicine, Houston, TX 77030, USA

²⁶Department of Neurosurgery, Texas Children's Hospital, Houston, TX 77030, USA

²⁷Dan L Duncan Comprehensive Cancer Center, Baylor College of Medicine, Houston, TX 77030, USA

²⁸These authors contributed equally

²⁹Lead contact

*Correspondence: mdt.cns@gmail.com (M.D.T.), xi.huang@sickkids.ca (X.H.)

<https://doi.org/10.1016/j.devcel.2025.01.001>

SUMMARY

Distinguishing tumor maintenance genes from initiation, progression, and passenger genes is critical for developing effective therapies. We employed a functional genomic approach using the Lazy Piggy transposon to identify tumor maintenance genes *in vivo* and applied this to sonic hedgehog (SHH) medulloblastoma (MB). Combining Lazy Piggy screening in mice and transcriptomic profiling of human MB, we identified the voltage-gated potassium channel *KCNB2* as a candidate maintenance driver. *KCNB2* governs cell volume of MB-propagating cells (MPCs), with *KCNB2* depletion causing osmotic swelling, decreased plasma membrane tension, and elevated endocytic internalization of epidermal growth factor receptor (EGFR),

thereby mitigating proliferation of MPCs to ultimately impair MB growth. *KCNB2* is largely dispensable for mouse development and *KCNB2* knockout synergizes with anti-SHH therapy in treating MB. These results demonstrate the utility of the Lazy Piggy functional genomic approach in identifying cancer maintenance drivers and elucidate a mechanism by which potassium homeostasis integrates biomechanical and biochemical signaling to promote MB aggression.

INTRODUCTION

Delineating the biological significance of genetic alterations across cancer genomes remains a challenge for target selection to develop effective therapies. Cancer genome alterations are classified as passengers or drivers.^{1,2} Passenger alterations do not contribute to tumor biology, while driver alterations actively contribute to tumorigenesis.^{3,4} Driver alterations may contribute to oncogenesis in distinct ways, often with different roles during the life cycle of cancer.^{5,6} Initiation genes are important for early malignant transformation, but may lose an active, causative role after tumor establishment.^{7,8} Progression genes promote further transformation of an established cancer, enhancing malignancy.^{9,10} The classical example of a progression driver is one that promotes metastatic dissemination.⁸ Maintenance drivers are required for the ongoing growth and survival of an established tumor. Importantly, neither initiation nor progression genes are necessarily required for tumor maintenance. We define maintenance genes as necessary for ongoing clonal maintenance, with loss of the maintenance gene resulting in clonal depletion. Therapeutic approaches targeting passenger, initiation, or progression genes are unlikely to be effective at regressing an established primary tumor. Due to the enormous financial, temporal, and human costs of developing therapies for pediatric cancer, selecting maintenance genes as targets for therapy development is a rational choice. The crux of the problem is therefore to identify such maintenance drivers.

Functional genomics, in which random and systematic mutagenesis across the genome is achieved, has been used to model cancer *in vivo* and identify the genes and pathways that contribute to oncogenesis.^{8,11–19} Forward genetic screens are typically performed in a sensitized genetic background, designed to identify genetic alterations which initiate or enhance tumorigenesis. However, such screens do not specifically identify genes which are essential for continued cancer cell survival after establishment of a tumor (i.e., the maintenance genes). Coupled with the difficulty in discerning maintenance genes from passenger, initiation, and progression genes, current *in vivo* screens require significant and resource-intensive functional validation of candidate genes. Medulloblastoma (MB) is the most common malignant pediatric brain tumor²⁰ and a major source of childhood morbidity and mortality. MB comprises four subgroups: WNT, sonic hedgehog (SHH), group 3, and group 4.²¹ Current standard-of-care for MB is non-targeted and includes maximal safe surgery, craniospinal radiotherapy, and cytotoxic chemotherapy.²² Long-term sequelae due to both disease and treatment markedly impairs quality of life in MB survivors.²³ SHH MB arises from over-activation of the SHH pathway in cerebellar granule neuron precursors (CGNPs) and encompasses 30% of all cases. SHH MB has been well

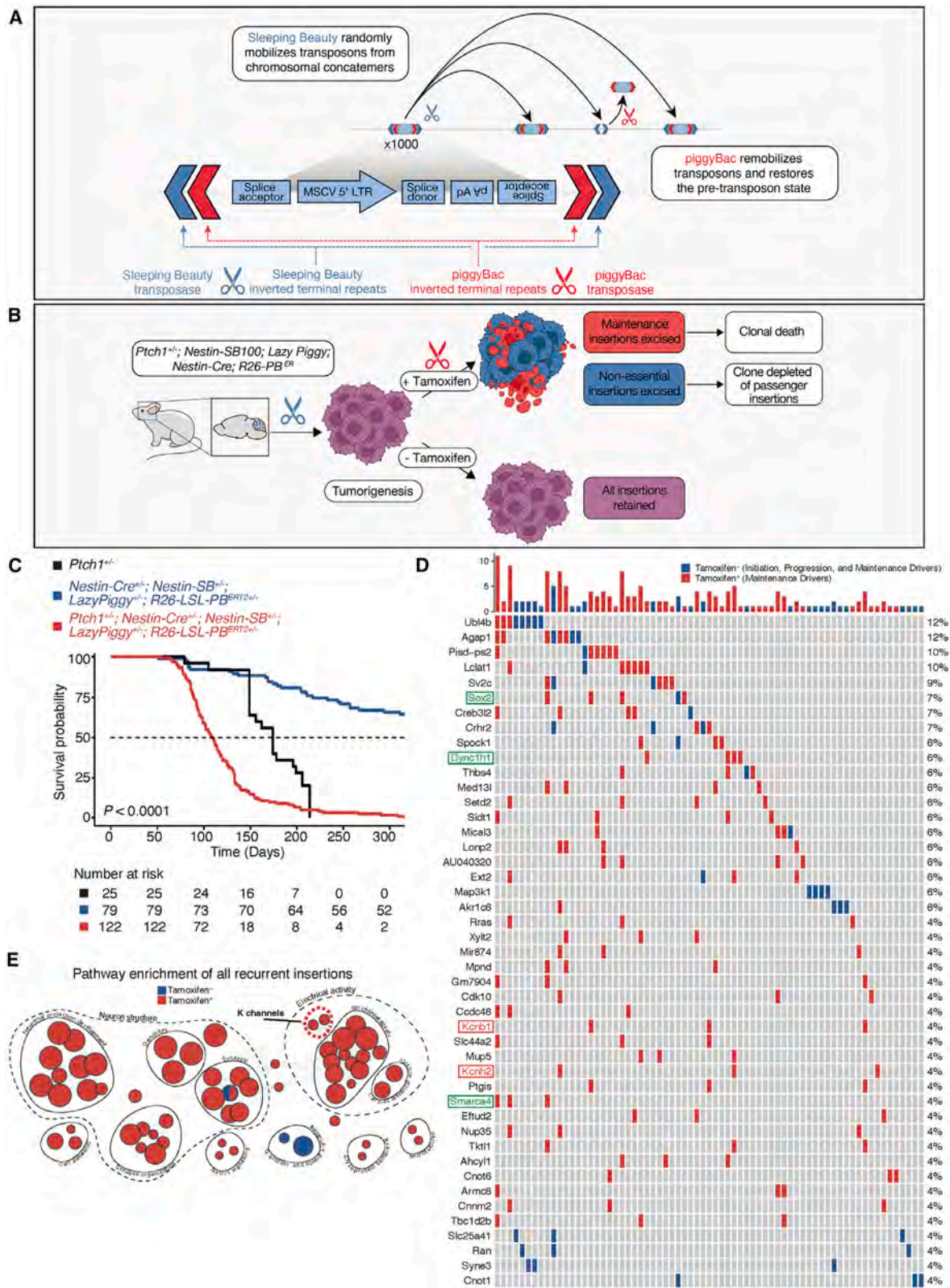
modeled by genetically engineered mouse models.^{24–28} Loss of one allele of the SHH pathway inhibitor *Ptch1* results in ~20% MB occurrence in mice.²⁴ *Math1-Cre; SmoM2* mice develop fully penetrant MB tumors due to expression of SmoM2 (the constitutively active form of the SHH pathway receptor Smo) driven by the CGNP-specific driver *Math1-Cre*.²⁷ As such, SHH MB offers an opportunity to identify maintenance genes through *in vivo* functional genomics.

To identify MB maintenance genes, we engineered an *in vivo* insertional mutagenesis screen using the nested, double jumping, Sleeping Beauty (SB)/piggyBac (PB) hybrid transposon, which we name Lazy Piggy. The Lazy Piggy system first dysregulates gene expression in neoplastic cells of MB-prone mice to enhance tumorigenesis and subsequently restores dysregulated gene expression to identify tumor clones harboring transposon insertions in maintenance genes. Combining Lazy Piggy screening in mice and transcriptomic profiling of human tumors nominated candidate maintenance genes in SHH MB, including the voltage-gated potassium channel *KCNB2*. Through comprehensive *in vitro* and *in vivo* studies, we validated the essential role of *KCNB2* and elucidated the mechanism by which *KCNB2* governs MB growth.

RESULTS

In vivo functional genomic screen for SHH MB maintenance genes

While the less efficient SB transposase drives transposition from donor concatemers, the more efficient PB transposase enables a higher remobilization rate from isolated solitary transposons in the genome.²⁹ Lazy Piggy is a modified version of the T2/Onc2 transposon¹² capable of dysregulating target gene expression, which we engineered to contain outer SB transposase recognition sites, with nested, inner PB transposase recognition sites (Figure 1A). This enables a functional genomic system in which two sequential screens can be performed in a single animal. SB transposase begins the first insertional mutagenesis screen to initiate cancer. SB transposase acts on the outer SB recognition sites of Lazy Piggy transposons located as concatemers on a donor chromosome to drive random and genome-wide transposition. After tumor establishment, delayed and inducible expression of the PB transposase enables a secondary positive selection screen via possible “remobilization” of singleton Lazy Piggy insertions across the genome. Remobilization (leading to excision and loss of the transposon insertion) of passenger, initiation, or progression events should have no effect on a given cell in the primary tumor, while remobilization from insertions in maintenance genes results in cellular death and clonal depletion (Figure 1B). SB-mediated insertions and PB-mediated excisions across the genome leave distinct “scars” composed of their respective inverted terminal repeats (Figures S1A and S3A) detectable by



(legend on next page)

PCR and next generation sequencing. By initiating tumors with the SB transposase (Figure S2) and then remobilizing the transposons in the established tumor using an inducible PB transposase, we can identify which mutational events are under positive selection and thus critical for ongoing tumor maintenance.

We generated a Lazy-Piggy-driven mouse model of SHH MB. Mice heterozygous for *Ptch1*, a negative regulator of the SHH pathway, sporadically develop MB with low latency.²⁴ Lazy Piggy mutagenesis (Figures S1A–S1F) is lineage restricted to neural progenitors of the developing mouse cerebellum by Nestin-driven SB transposase (*Nestin:Luc-SB100*) and temporally regulated by tamoxifen-inducible PB transposase (*Nestin-Cre; R26-LSL-mPB-ER^{T2}*). Lazy Piggy mutagenesis generated a highly penetrant model of SHH MB in quintuple transgenic mice, (*Ptch1^{+/-}; Nestin:Luc-SB100^{+/-}; Lazy Piggy^{+/-}; Nestin-Cre^{+/-}; R26-LSL-PB^{ERT2+/-}*) as compared with control parental *Ptch1^{+/-}* mice, or quadruple transgenic mice lacking the *Ptch1^{+/-}* allele (*Nestin:Luc-SB100^{+/-}; Lazy Piggy^{+/-}; Nestin-Cre^{+/-}; R26-LSL-PB^{ERT2+/-}*) (Figures 1C and S1G). Acceleration of the brain tumor phenotype (and death) in *Ptch1^{+/-}; Nestin:Luc-SB100^{+/-}; Lazy Piggy^{+/-}; Nestin-Cre^{+/-}; R26-LSL-PB^{ERT2+/-}* as compared with *Ptch1^{+/-}* control animals confirms that Lazy Piggy transposition driven by the SB transposase in the Nestin compartment drives MB formation in this animal model (Figure 1C). As such, we conclude that in quintuple mice, a subset of Lazy Piggy transposon insertions are driver events.

After tumor initiation, tracked by either bioluminescence or visible cranial bulging (Figures S1H and S1I), low-dose tamoxifen was administered to a subset of animals to activate the PB transposase (Figure S1J). Nuclear translocation of PB transposase protein enables excision and removal of a subset of Lazy Piggy insertions dispersed across the genome by the SB transposase as singleton transposons. Low-dose tamoxifen treatment confers minimal survival benefit (Figure S1K) and is not curative, as either depleting a minority of maintenance insertion-containing clones or subclonal remobilization of a given maintenance insertion would be replenished by continued growth of remaining tumor clones with intact maintenance insertions. As such, we expect enrichment for maintenance insertions across the tumor bulk following depletion of non-essential insertions. To account for donor chromosome insertion bias, we generated separate founder mice harboring Lazy Piggy concatemers on chromosomes 7 and 10 (Figures S1L and S1M). Restriction-splink PCR^{30,31} and gene-

centric common insertion site (gCIS) analysis³² were used to determine the genes where Lazy Piggy insertions are more common than would be expected by random chance from 69 tumors with (TAM⁺) and without (TAM⁻) tamoxifen-induced secondary mobilizations. This enables the identification of specific transposon insertions that may be required for ongoing tumor maintenance (Figure 1D). Splink libraries were also generated using primers specific to PB excision scars to identify sites of secondary mobilization. The overlap of these sites with the set of all SB insertions was used to assess robustness of tamoxifen-induced remobilization quantified per tumor (Figures S3A–S3C).

Lazy Piggy screen implicates potassium channels in MB maintenance

To validate candidates identified by the Lazy Piggy screen, we first analyzed whole-genome CRISPR screening results from The Cancer Dependency Map (DepMap), an ongoing project which characterizes gene dependencies in hundreds of cancer cell lines including MB cells.³³ Several Lazy Piggy screen hits (*AHCYL1*, *DYNC1H1*, *EFTUD2*, and *SMARCA4*) are dependencies in MB (Figure 2A). Among these, *DYNC1H1* and *AHCYL1* are MB dependencies that are not overexpressed in SHH MB (Figure 2B). Gene expression and dependency are not necessarily linked, highlighting the utility of functional genomics in finding targets that are functional but not overexpressed in cancer. Furthermore, we corroborated these dependencies by performing small interfering RNA (siRNA)-mediated knockdown of *AHCYL1*, *DYNC1H1*, and *SMARCA4* in ONS76 human MB cells, which all significantly impaired MB cell growth (Figures 2D, 2F, and S3J). Among the insertions that persisted despite transposon remobilization, there was a notable enrichment of the voltage-gated potassium channel gene family, represented by the genes *Kcnb1* and *Kcnh2* (Figures 1D and S3D–S3G). Additionally, pathway enrichment analysis of all recurrently inserted genes identified enrichment terms for electrical activity and potassium channels, both restricted to the TAM⁺ (PB-remobilized) tumor population (Figure 1E). siRNA-mediated depletion of *KCNB1* and *KCNH2* impaired MB cell growth relative to non-targeting controls (Figures 2D and 2F), and cell volume increases were only observed upon depletion of these two potassium channel genes in the validation panel (Figures 2C, 2E, and S3I). These results suggest that large scale genome-wide screens such as DepMap may not effectively capture dependencies on potassium channel

Figure 1. Functional genomic identification of cancer maintenance drivers using the Lazy Piggy transposon

(A) Tumorigenesis begins as Sleeping Beauty (SB100, blue scissors) mobilizes the transposon to induce genome-wide mutagenesis. Second, low-dose tamoxifen induces piggyBac (PB, red scissors)-mediated remobilization and excision in a minority of transposon insertions, restoring the original gene function of select insertion events.

(B) Due to remobilization, insertions at passenger, initiation, and progression genes are depleted with no consequence to tumor survival or clonal architecture of the tumor. However, transposon remobilization from maintenance drivers results in clonal death. Surviving clones after remobilization are therefore enriched for insertions at maintenance drivers.

(C) *Ptch1^{+/-}* mice with Lazy Piggy transposition experienced diminished overall survival compared with *Ptch1^{+/-}* mice, and *Ptch1^{+/+}* mice with Lazy Piggy transposition alone. To induce transposon secondary mobilization by PB-ERT2, low-dose tamoxifen chow was administered following visualization of cranial tumor bulge.

(D) Significant gCIS candidates from all sequenced samples ($n = 69$) comprising tamoxifen-negative tumors (blue) with parental insertions that have not been remobilized, and tamoxifen-treated tumors (red) with maintenance driver insertions enriched through piggyBac-mediated transposon remobilization. Green boxes indicate recovery of known MB drivers *Sox2*, *Dync1h1*, and *Smarca4*. Red boxes indicate recurrent gCIS in potassium channel genes *Kcnb1* and *Kcnh2*.

(E) gProfiler pathway enrichment of all recurrent gCIS candidates (≥ 2 tumors). Nodes represent enrichment terms, where terms with 10–500 genes and $Q < 0.05$ are shown, and node size determined by the number of genes. A noted enrichment for ion channel activity, particularly potassium channels, is seen among the remobilized tumors (maintenance events).

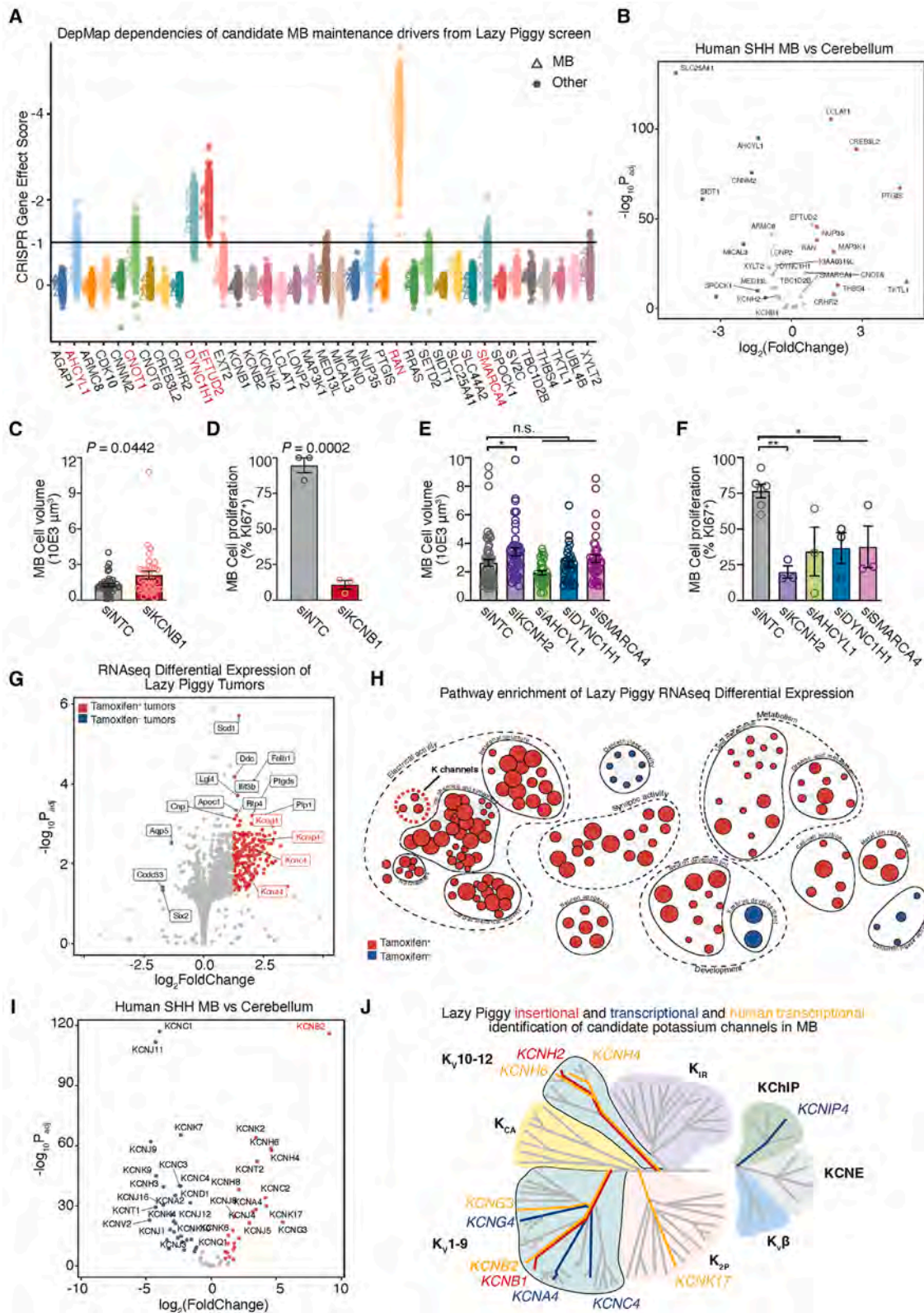


Figure 2. Lazy Piggy screening implicates potassium channels in SHH MB maintenance

(A) Analysis of Lazy Piggy candidate gene dependency in DepMap. Each point represents a distinct cell line, grouped as either MB or all other tumor types. A gene effect score of -1 or less can be interpreted to mean that a particular gene is essential for proliferation of the corresponding cell line.³³

(legend continued on next page)

genes, and that potassium channels may regulate MB cell fitness through a convergent mechanism of cell volume regulation.

Beyond the detection of *Kcnb1* and *Kcnh2* gCIS, bulk RNA sequencing (RNA-seq) reveals highly upregulated expression of additional potassium channel genes (*Kcng4*, *Kcnip4*, *Kcnc4*, and *Kcna4*) restricted to TAM⁺ remobilized Lazy-Piggy-driven tumors by both gene expression and pathway analysis (Figures 2G and 2H). Low-dose tamoxifen treatment should revert dysregulated gene expression at non-maintenance insertions and thus enrich for transcription of essential maintenance genes and mechanisms. As such, transcriptional upregulation in TAM⁺ tumors highlights potassium channel activity as a putative MB maintenance mechanism. As potassium channels are membrane localized and represent promising druggable targets for treating human disease, they were chosen for further study.

While ion channels are attractive therapeutic targets,^{38–40} it is critical to identify potassium channels with MB-specific function. *Kcnb1* knockout mice are hyperactive and prone to seizures.^{41,42} *KCNB1* mutations are implicated in epileptic encephalopathy⁴³ and neurodevelopmental disorders⁴⁴ in humans. *KCNH2* is a critical mediator of cardiac action potential and its dysfunction can result in fatal cardiac arrhythmias.⁴⁵ Given the important functions of *KCNB1* and *KCNH2* in normal physiology, we studied potassium channel expression in human MB transcriptomes to more broadly identify targets. We identified *KCNB2*, a human paralog of *Kcnb1*, as the top upregulated potassium channel in human SHH MB relative to normal cerebellum (Figure 2I). Taken together, Lazy Piggy functional genomics reveal the importance of potassium channel function for MB maintenance (Figure 2J). Orthogonal transcriptomic analysis of human tumors nominates *KCNB2* for further investigation in SHH MB.

***Kcnb2* is dispensable for mouse development**

Since potassium channels have pleiotropic effects in human physiology, including critically in the myocardium, we investigated whether *KCNB2* could serve as a drug target.⁴⁴ We examined the developmental phenotype of global *Kcnb2* knockout mice (Figures S4A–S4K). *Kcnb2*^{−/−} mice are viable (Figure S4A) and produce offspring at expected Mendelian ratios (Figure S4B). No defects in body weight at weaning (Figure S4C), litter size (Figure S4D), gross morphology (Figure S4E), or brain morphology

were observed (Figures S4F and S4G). We observed no overt differences in the cerebellar architecture of *Kcnb2*^{−/−} mice at postnatal day 7 or 30 (P7 and P30) (Figures S4H–S4K). Analysis of a mouse phenotyping database^{46,47} reveals that *Kcnb2* knockout mice display hyperactivity, but major internal organ morphology and function are unaffected. Genotype-Tissue Expression (GTEx) bulk tissue RNA-seq data reveal human *KCNB2* expression in the brain, esophagus, pituitary, spleen, and thymus (Figure S4L). Beyond the brain, tissue-specific *KCNB2* function in other organs has not been thoroughly investigated. There are no reported associations between *KCNB2* mutations with human pathogenic disease in the ClinVar database. However, a recent study identified seven individuals with neurodevelopmental delay with monoallelic inactivation of *KCNB2*, associated with increased neuronal hyperexcitability.⁴⁸ By comparison, over 29 distinct pathogenic *KCNB1* variants have been identified in individuals suffering from early-onset developmental and epileptic encephalopathies.^{43,49} Taken together, these data indicate that *Kcnb2* is non-essential for normal development and organ physiology in mice. *KCNB1* variants appear to more frequently contribute to human pathogenesis compared with *KCNB2*. While we investigated the functional roles of *KCNB2* in regulating MB, discerning *KCNB2* function in neuronal development and organ function using conditional mouse mutants or relevant human tissues and cell types *ex vivo* will be critical to further assess the safety profile of *KCNB2* as a pediatric cancer target.

***Kcnb2* is required for stage-dependent proliferative expansion of MPCs**

To validate the maintenance role of *KCNB2* in SHH MB, we crossed *Kcnb2*^{−/−} mice with SHH MB-prone *Math1-Cre*; *R26-LSL-SmoM2-eYFP* mice.^{25,26} *KCNB2* deficiency prolongs the survival and reduces tumor burden of SHH MB-bearing mice in an allele dose-dependent manner (Figures 3A and 3B). Consistent with a role in MB maintenance, *KCNB2* does not impact tumor initiation as all control and *KCNB2*-deficient tumor-bearing mice succumb to MB (Figure 3A). SHH MB has a well characterized hierarchical cellular structure, with apical SOX2⁺ stem cells (MB-propagating cells [MPCs]) that give rise to DCX⁺ transit-amplifying progenitor cells, which subsequently give rise to post-mitotic NEUN⁺ cells.^{50,51}

(B) RNA-seq differential expression of Lazy Piggy hits in published human SHH MB ($n = 182$) versus human control cerebellum ($n = 9$).^{34–37}

(C) Cell volume quantification of ONS76 MB cell volume upon siRNA-mediated *KCNB1* knockdown. *KCNB1* depletion significantly increases MB cell size relative to non-targeting control (NTC).

(D) Quantification of ONS76 MB cell proliferation by KI67 positivity upon siRNA-mediated *KCNB1* knockdown. *KCNB1* depletion significantly reduces MB cell proliferation relative to siNTC.

(E) Cell volume quantification of ONS76 MB cell volume upon siRNA-mediated knockdown of *KCNH2*, *AHCYL1*, *DYNC1H1*, and *SMARCA4*. Only depletion of potassium channel *KCNH2* led to an increase in cell volume. "ns" denotes $p > 0.05$, * denotes $p \leq 0.05$.

(F) Quantification of ONS76 MB cell proliferation by KI67 positivity upon siRNA-mediated knockdown of *KCNH2*, *AHCYL1*, *DYNC1H1*, and *SMARCA4*. * denotes $p \leq 0.05$, ** denotes $p \leq 0.01$.

(G) RNA-seq differential expression of tamoxifen-treated versus untreated Lazy Piggy tumors. Red and blue dots represent genes upregulated in tamoxifen-treated and -untreated tumors, respectively. Outlier gene *Scd2* omitted for visualization (\log_2FC 0.49; p_{adj} $1e-11$). Potassium channel genes demonstrate increased expression among the tamoxifen-treated tumors compared with untreated tumors.

(H) gProfiler pathway enrichment of RNA-seq differentially expressed genes between tamoxifen-treated and -untreated Lazy Piggy tumors. Nodes represent enrichment terms, where terms with 10–500 genes and $Q < 0.05$ are shown, and node size determined by the number of genes. Pathway enrichment for ion channels, particularly potassium channels, is observed.

(I) RNA-seq differential expression of potassium channels in published human SHH MB ($n = 182$) versus human control cerebellum ($n = 9$).^{34–37} The most highly expressed potassium channel in tamoxifen-treated versus untreated tumors is *KCNB2*, a paralog of the gCIS *Kcnb1*.

(J) Phylogeny illustrating potassium channel classes (bold) and genes identified from Lazy Piggy and human patient expression analysis. *Kcnb1* and *Kcnb2* are nearest neighbors.

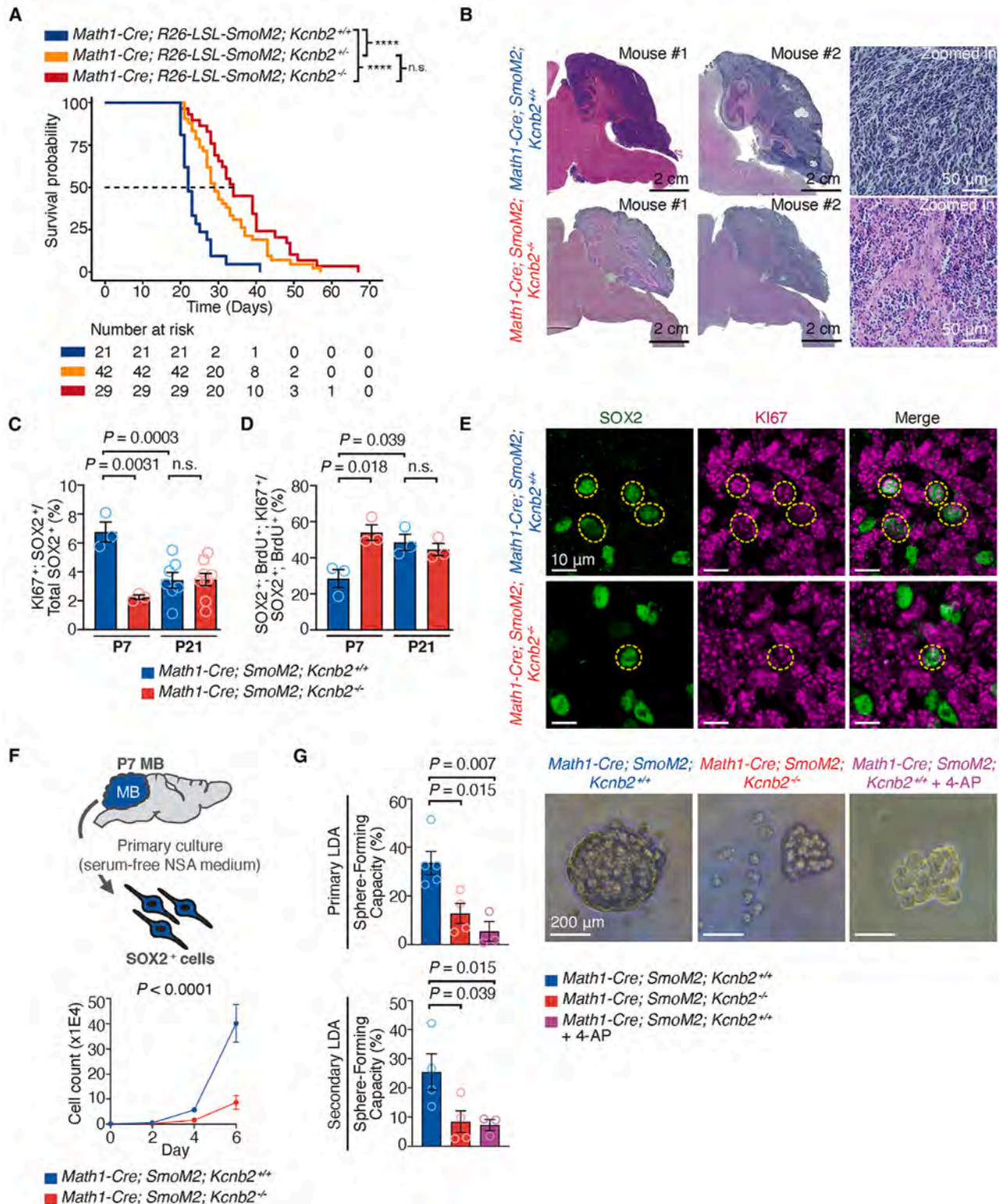


Figure 3. *Kcnb2* deficiency prolongs survival and reduces tumor burden of SHH MB-bearing mice

(A) Overall survival in *Math1-Cre; R26-LSL-SmoM2* MB-bearing mice, on the background of *Kcnb2*^{+/+}, *Kcnb2*^{+/-}, or *Kcnb2*^{-/-} alleles. "ns" denotes $p > 0.05$, **** denotes $p \leq 0.0001$.

(B) Representative histology of sagittal sections from age-matched P21 *Math1-Cre; R26-LSL-SmoM2* MB-bearing mice with *Kcnb2*^{+/+} or *Kcnb2*^{-/-} alleles.

(legend continued on next page)

Kcnc2 is expressed in *Sox2*⁺ and *Dcx*⁺ cells from mouse and human SHH MB, as documented by single-cell RNA-seq data (Figures S5A and S5B)^{52–54} and single-molecule *in situ* hybridization (Figures S5C and S5D). The cellular hierarchy is unperturbed in *Kcnc2*^{−/−} tumors (Figures S5E–S5J), though there is a diminished population of SOX2⁺ MPCs in late-stage (P21) *Kcnc2*^{−/−} tumors (Figures S5K–S5N) that was not attributable to changes in overall mitotic index (Figures S5O and S5P) or apoptosis (Figures S5Q–S5S). KCNC2 deficiency decreases the proliferating MPC fraction (Figures 3C and 3E). Bromodeoxyuridine (BrdU) pulse-chase analysis (Figure S5T) revealed that KCNC2 knockout delays cell-cycle progression (Figure 3D) and specifically prolongs S-phase duration (Figure S5U) of MPCs in early-stage (P7) tumors, while this effect is diminished in their DCX⁺ progeny (Figures S5V–S5X). Consistent with this, MPCs isolated from *Kcnc2*^{−/−} tumors display impaired *in vitro* growth (Figure 3F) and primary and secondary sphere-forming capacity (Figure 3G).⁵⁵ Pharmacologic blockade of voltage-gated potassium channels with 4-aminopyridine (4-AP) likewise impairs sphere-forming capacity (Figure 3G). Collectively, these data demonstrate that KCNC2 is cell-autonomously required for MPC proliferation.

KCNC2 regulates potassium homeostasis and mechanical properties of MPCs

We hypothesized that the proliferation defect in *Kcnc2*^{−/−} tumors was due to altered potassium flow across the cell membrane. Whole-cell patch clamp recordings demonstrate that KCNC2 deficiency reduces potassium currents across the cell membrane in MPCs (Figures 4A–4C) and increases cell capacitance (Figure 4D), which is associated with an increase in membrane surface area and increase in cell volume (Figure 4F).⁵⁶ Thus, KCNC2 deficiency elevates intracellular potassium ion concentration, promoting the osmotic influx of water with subsequent cell swelling.

We next tested whether increased osmotic swelling may disrupt the balance of biomechanical forces in cancer cells. Increased cell swelling may be due to inner cell pressure, a rounding force which pushes outward against the plasma membrane. Increased cell swelling could also affect plasma membrane tension, the in-plane force which counteracts surface expansion (Figure 4E). Atomic force microscopy and micropipette aspiration demonstrates that KCNC2 deficiency has no discernible effect on inner cell pressure (Figure 4G) but significantly reduces plasma membrane tension in SOX2⁺ MPCs (Figure 4H). Previous studies associate increased cell volume from acute pharmacological perturbations with increased membrane tension.^{57–59} While acute hypo-osmotic shock rapidly increases MPC membrane tension (Figure 4I), under chronic hypo-osmotic

conditions, MPCs adapt to restore comparable membrane tension values compared with the control isotonic condition (Figure 4J). Furthermore, broad pharmacologic blockade of potassium currents with tetraethylammonium (TEA), or specific blockade of voltage-gated potassium currents with 4-AP increases cell volume and reduces plasma membrane tension in KCNC2 wild-type MPCs (Figures 4K–4M). Together, these data indicate that in response to cell swelling, engagement of distinct compensatory mechanisms depends on the duration (acute or chronic), modality (genetic or pharmacological), and nature (potassium channel perturbation or ionic homeostasis) of hypo-osmotic shock. We conclude that KCNC2 regulates intracellular potassium ion concentration, thereby controlling the volume and plasma membrane tension of MPCs.

KCNC2-mediated actin-membrane tethering regulates membrane tension to govern EGFR endocytosis

As membrane tethering to the intracellular actin cortex contributes to membrane tension, we hypothesized that KCNC2 might influence plasma membrane tension and actin-membrane tethering through changes in osmolarity.⁶⁰ We cultured MPCs in hyper-, hypo-, and isotonic conditions and measured actin-plasma membrane tethering by colocalization of phosphorylated ezrin, radixin, moesin (pERM) proteins with F-actin (Figure 5A). We observed reduced tethering in KCNC2-deficient versus wild-type MPCs and that hypertonic conditions rescue both tethering defects and concomitant changes in cell size (Figures 5B, 5C, S6A, and S6B). Membrane tethering was not further altered for KCNC2 wild-type MPCs in hypertonic conditions, nor for KCNC2-deficient MPCs in hypotonic conditions, suggesting that osmolar gradients govern membrane tethering within a limited biological range. Since membrane tension and pERM tethering rise during mitosis to facilitate cell rounding and spindle positioning,^{60,61} the proliferation defects in KCNC2-deficient MPCs (Figures 3C–3E) may be attributed to the biomechanical consequences of impaired potassium homeostasis.

A more flexible plasma membrane with reduced membrane tension facilitates endocytosis, which occurs mainly through Clathrin- and caveolae-dependent pathways.^{62–64} *Kcnc2*^{−/−} MPCs display increased Caveolin-1⁺ and Clathrin⁺ puncta, as well as increased Rab5⁺ puncta, a marker of early endosomes (Figure 5D). Endocytosis can regulate the signaling output of receptor tyrosine kinases (RTKs).⁶⁵ Brain tumor-propagating cells are traditionally maintained with epidermal growth factor (EGF) and fibroblast growth factor (FGF), which activate downstream RTKs.⁶⁶ We hypothesized that KCNC2 may regulate EGF or FGF signaling to govern MB cell proliferation. Growth factor titration experiments illustrated that MPC viability is more crucially dependent on EGF than FGF (Figure S6C).⁶⁶ We surveyed

(C) Quantification of KI67⁺ cycling proportion of SOX2⁺ MPCs at P7 and P21. Loss of *Kcnc2* function is associated with decreased cycling fraction of SOX2⁺ cells at P7 but not P21, suggesting the proliferative capacity of SOX2⁺ cells is already diminished at this time point.

(D) Quantification of SOX2⁺ cell-cycle retention at P7 and P21. Loss of *Kcnc2* increases cell-cycle retention of P7 MPCs, but not at P21.

(E) Representative images of SOX2 and KI67 immunohistochemistry from P7 MBs.

(F) Top: schematic for isolation and culture of SOX2⁺ MPCs. Bottom: 6-day cell counting assay comparing *Kcnc2*^{+/+} versus *Kcnc2*^{−/−} MPCs demonstrates decreased growth after *Kcnc2* loss of function.

(G) Representative microscopy and sphere-forming limiting dilution analyses (LDAs) of SHH MB tumor spheres of *Kcnc2*^{+/+} versus *Kcnc2*^{−/−} with or without 2.5 mM 4-aminopyridine (4-AP) blockade of voltage-gated potassium channels. Either genetic *Kcnc2* deletion or pharmacologic inhibition of voltage-gated potassium currents is detrimental to the growth of SHH MPCs.

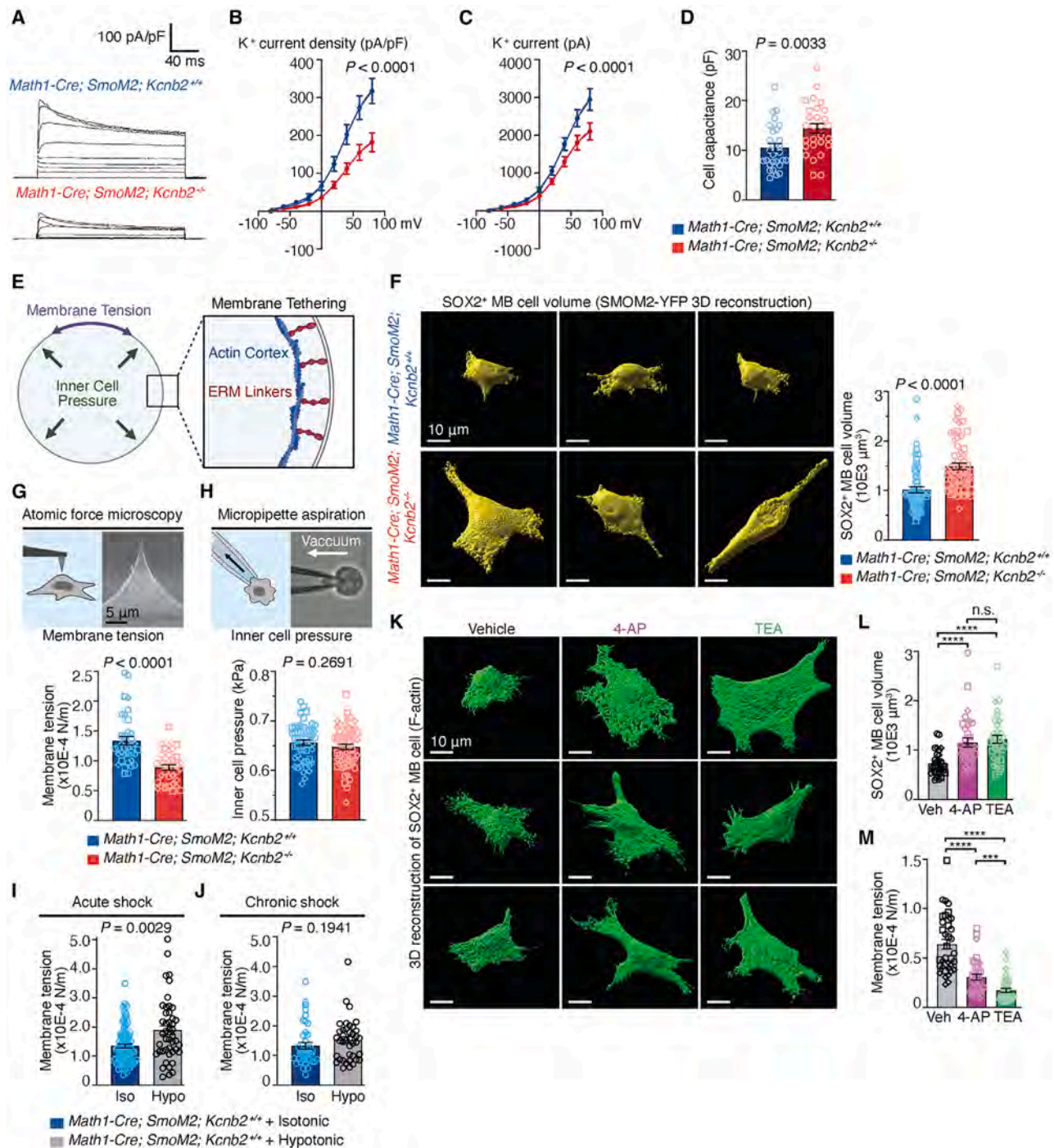


Figure 4. *Kcnb2* regulates cell membrane tension of MPCs

(A) Representative current traces show total currents from whole-cell recordings of SOX2⁺ SHH MPCs, with or without *Kcnb2* loss. Currents are elicited by voltage steps from -80 to 80 mV in 20-mV increments. Total current is attenuated in the absence of *Kcnb2*.

(B) Current-voltage (I-V) curves of *Kcnb2*^{+/+} versus *Kcnb2*^{-/-} SHH MPCs.

(C) Total potassium current (pA) curves of *Kcnb2*^{+/+} versus *Kcnb2*^{-/-} SHH MPCs.

(D) Cell capacitance of *Kcnb2*^{+/+} versus *Kcnb2*^{-/-} SHH MPCs.

(E) Schematic illustrating concepts of membrane tension, inner cell pressure, and membrane tethering.

(F) 3D-reconstruction (left) and quantification (right) of SOX2⁺ SHH MPC volume as measured by SmoM2-YFP signal demonstrates larger cell volumes in the absence of *Kcnb2*.

(G) Apparent membrane tension analysis of *Kcnb2*^{+/+} versus *Kcnb2*^{-/-} SHH MPCs. (Top) Schematic and images shown for the probes used for atomic force microscopy experiments. Membrane tension is diminished in the absence of *Kcnb2*.

(legend continued on next page)

global RTK activation in MPCs through a phospho-RTK array, demonstrating activation (phosphorylation) of EGF receptor (EGFR) family members EGFR and ERBB2 (Figures 5E, S6D, and S6E).

Compared with control MPCs, KCNB2-deficient MPCs exhibit increased colocalization of phosphorylated EGFR (pEGFR) with Caveolin-1⁺ puncta and reduced overall pEGFR, suggesting increased pEGFR endocytosis (Figures 5E–5I, S6A, and S7A). Conversely, pERBB2 signal was not significantly altered (Figure 5E). Bulk RNA-seq of *Math1-Cre; R26-LSL-SmoM2* and *Math1-Cre; R26-LSL-SmoM2; Kcnc2^{-/-}* tumors reveals EGFR being among the top downregulated RTK genes following KCNB2 knockout (Figures S7A–S7C), demonstrating dysregulation of EGFR at both protein and transcript levels. Furthermore, we performed total internal reflection fluorescence microscopy, which visualizes plasma-membrane-localized molecules. Plasma-membrane-localized Caveolin-1 increases and pEGFR decreases with KCNB2 deficiency (Figure 5J). Furthermore, we corroborated these findings *in vivo* by immunohistochemistry of early-stage (P7) *Math1-Cre; R26-LSL-SmoM2* tumors, where we observed that KCNB2 knockout decreases pERM, increases Caveolin-1, and decreases pEGFR in SOX2⁺ MPCs (Figures 6A and 6B). We conclude that control of membrane tension through KCNB2 regulation of intracellular potassium and cell volume sustains high level EGFR signaling, which supports MPC proliferation, illustrating the molecular and biophysical mechanism by which loss of KCNB2 impairs the growth of SHH MB.

To interrogate this relationship, we manipulated membrane tension while monitoring endocytosis and EGFR signaling (Figure 6C). NSC668394, an inhibitor of Ezrin phosphorylation, reduces actin-plasma membrane tethering to decrease membrane tension.^{63,67} Methyl- β -cyclodextrin (M β CD) depletes cholesterol from the plasma membrane to increase membrane tension.^{63,68,69} Treating control MPCs with NSC668394 phenocopies *Kcnc2* knockout, increases cell size, elevates Caveolin-1 expression, and reduces pEGFR signal (Figure 6D). Conversely, treating *Kcnc2^{-/-}* MPCs with M β CD reduces cell size, decreases Caveolin-1 expression, and increases pEGFR signal (Figure 6E). This demonstrates that at least in part, KCNB2 supports MPC growth through regulating plasma membrane tension to control EGFR endocytosis, thereby boosting EGFR signaling.

To further validate this model, we attempted to rescue the proliferation defect of *Kcnc2^{-/-}* MPCs through manipulation of membrane tension with its effects on EGFR endocytosis and signaling. KCNB2 knockout MPCs have diminished proliferation *in vitro* (Figure 6F), comparable to control MPCs cultured in EGF-deficient media (from 10 to 1 ng/mL). Supplementation with EGF ligand (from 10 to 20 ng/mL) is sufficient to rescue proliferation of

Kcnc2^{-/-} MPCs to control levels. Pharmacologic increase in membrane tension with M β CD further increased BrdU incorporation, suggesting that high membrane tension cooperates with EGF ligands to facilitate MPC proliferation. KCNB2 overexpression reduces the volume of ONS76 MB cells (Figures S7D and S7E) while increasing cell proliferation and EGFR phosphorylation (Figures S7F–S7H). We conclude that KCNB2 is necessary and sufficient to promote SHH MB growth by integrating potassium efflux, osmotic cell swelling, and membrane tension to regulate EGFR endocytosis and the mitogenic EGFR signaling.

KCNB2 deficiency synergizes with SHH inhibition in treating MB

Prior studies demonstrated that while vismodegib, a clinically approved SHH pathway antagonist,⁷⁰ debulks SHH MB by targeting the rapidly cycling DCX⁺ MB cells, refractory stem-like SOX2⁺ MB cells remain.^{50,71} This suggests that mitigating SHH MB growth requires targeting both MPCs and the proliferative tumor bulk. Since *Kcnc2* loss impairs SOX2⁺ MPC expansion, we sought to investigate whether targeting KCNB2 synergizes with SHH pathway inhibition in treating MB. First, we determined that KCNB2 loss does not sensitize MPCs to vismodegib *in vitro* (Figure 6G). We then tested the utility of vismodegib in mice with SHH MB that were proficient or deficient for KCNB2. Vismodegib alone did not improve survival compared with a vehicle control in *Kcnc2* wild-type mice, consistent with previous literature.⁷¹ In contrast, vismodegib treatment significantly prolonged the survival of *Kcnc2^{-/-}* mice with SHH MB (Figure 6H). These findings support KCNB2 as a maintenance driver in SHH MB and that clinical trials of KCNB2 inhibition in children with SHH MB are warranted.

DISCUSSION

To identify optimal targets for cancer therapies, we developed a functional genomic tool, the “double-jumping” transposon Lazy Piggy. This tool leverages the differential transposition efficiencies of SB and PB transposases—SB being less efficient and primarily driving transposition from donor concatemers, while PB is more efficient and allows for higher remobilization rates.²⁹ SB-mediated transposon insertions in maintenance genes both drive tumorigenesis and are essential for ongoing maintenance of the established tumor.⁷² Such maintenance insertions are under positive selection and cannot be removed by delayed secondary PB-mediated transposition. Thus, identification of essential maintenance-driving transposon insertions nominates candidate genes for therapeutic targeting. Our application of Lazy Piggy in a genetically engineered mouse model of

(H) Inner cell pressure analysis of *Kcnc2^{+/+}* versus *Kcnc2^{-/-}* SHH MPCs demonstrates no differences. (Top) Schematic and images show micropipette aspiration technique used.

(I) Apparent membrane tension analysis of *Kcnc2^{+/+}* SHH MPCs in isotonic conditions (360 mOsm) or immediately after hypotonic shock (250 mOsm: normal media + 30% de-ionized water). Acute hypo-osmotic shock drives MPC membrane tension increase.

(J) Apparent membrane tension analysis of *Kcnc2^{+/+}* SHH MPCs in isotonic conditions (360 mOsm) or after 1 week of hypotonic stress (250 mOsm: normal media + 30% de-ionized water). Under chronic hypo-osmotic conditions, MPCs no longer have significantly elevated membrane tension relative to isotonic controls.

(K–M) Representative images of SOX2⁺ SHH MPCs with voltage-gated blockade (2.5 mM 4-AP) or broad blockade (5 mM tetraethylammonium [TEA]) of potassium channels, with quantification of SOX2⁺ MPC volume (L) as measured by α -tubulin signal and apparent membrane tension of SOX2⁺ SHH MPCs (M). Cell volume is increased, and membrane tension decreased after potassium channel blockade. “ns” denotes $p > 0.05$, *** denotes $p \leq 0.001$, **** denotes $p \leq 0.0001$.

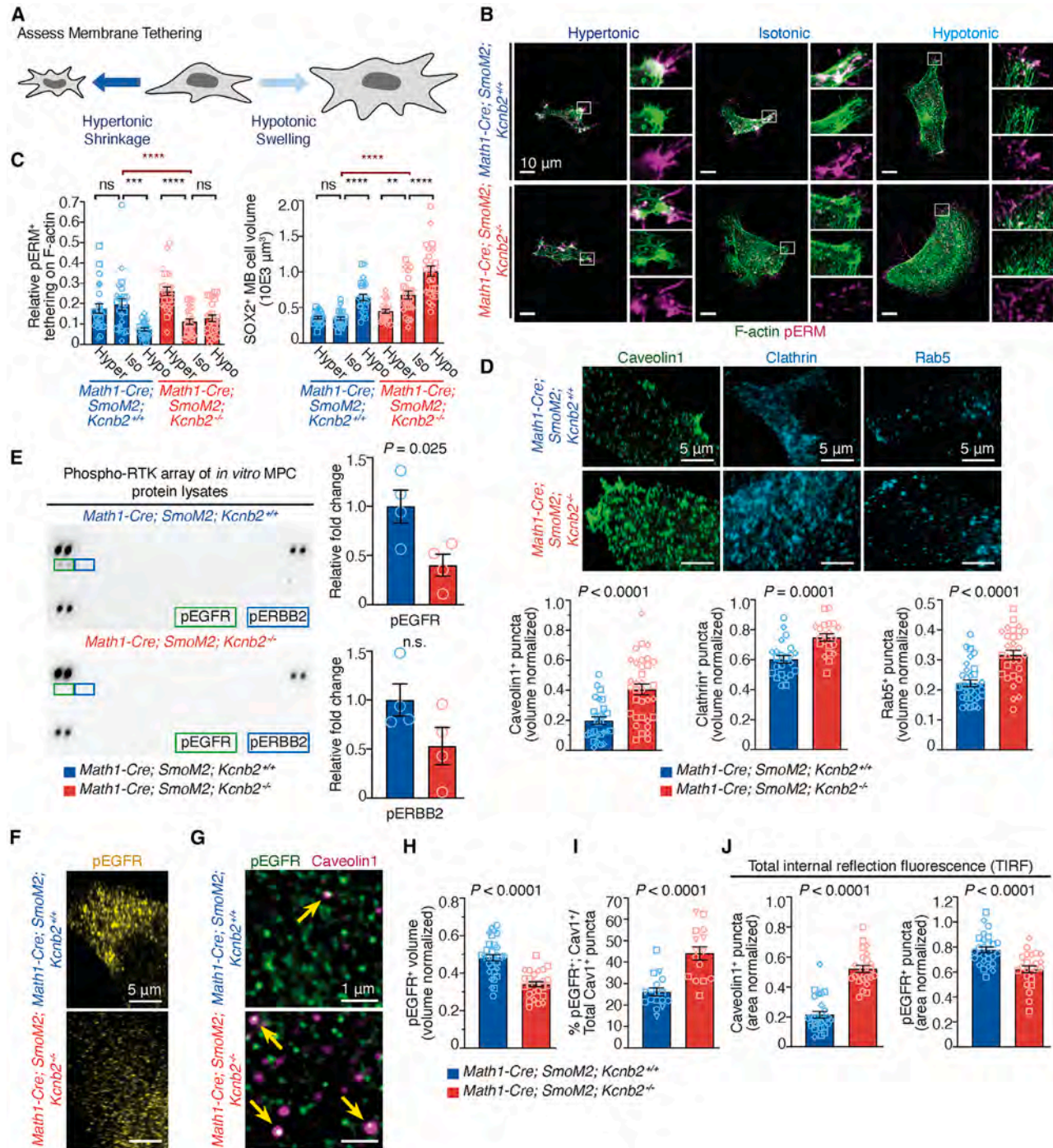


Figure 5. KCNB2 regulates the endocytosis of EGFR in SHH MPCs

(A) Experimental schematic outlining osmolarity manipulation to assess membrane tethering.

(B and C) Representative immunocytochemistry (B) and quantification (C) of pERM membrane tethering and cell size in KCNB2 wild-type and knockout MPCs under hypertonic, isotonic, and hypotonic conditions. Relative tethering is measured by co-localized pERM⁺; F-actin⁺ signal normalized to total F-actin⁺ volume (left) and cell size by SmoM2-YFP volume (right). Hypertonic conditions were achieved by addition of 3.75% polyethylene glycol (PEG) 1,500 for 24 h. Hypotonic conditions were achieved by addition of 30% de-ionized water for 24 h. Loss of function of *Kcnb2* results in larger cells in response to hypotonic fluids, and decreased membrane tethering. "ns" denotes *p* > 0.05, * denotes *p* ≤ 0.05, ** denotes *p* ≤ 0.01, *** denotes *p* ≤ 0.001, and **** denotes *p* ≤ 0.0001.

(D) Representative images and quantification of endocytic markers Caveolin-1, Clathrin, and Rab5 in SOX2⁺ SHH MPCs demonstrates increased staining for endocytic markers in the absence of *Kcnb2*.

(E) Representative images and quantification of detectable phosphorylated EGFR (pEGFR) and phosphorylated ERBB2 (pERBB2) signal from phospho-RTK array analysis of SOX2⁺ SHH MPC lysates demonstrates diminished pEGFR in the absence of KCNB2.

(legend continued on next page)

SHH MB demonstrated its capability to reveal both known maintenance drivers, as well as previously uncharacterized candidate maintenance drivers for future investigation. *TKTL1* is the most differentially upregulated candidate maintenance driver in human MB (Figure 2B) identified in our forward genetic screen (Figure 1D). *TKTL1* is associated with tumor proliferation^{73,74} and its human ortholog specifically promotes expanded neurogenesis of basal radial glia,⁷⁵ which are cortical progenitors analogous to the cerebellar granule cell precursor cell-of-origin of SHH MB.

Lazy Piggy technology can be used across multiple cancer lineages to not only identify cancer drivers but also for targeting maintenance genes, which we contend are the optimal targets for treatment design. Sequencing of cancer genomes and functional genomic approaches have greatly expanded our understanding of cancer biology and, in some cases, have identified effective targets and strategies for treating a subset of cancers.⁷⁶ Our Lazy Piggy approach is a valuable addition to this arsenal, particularly for selecting targets that are crucial for tumor maintenance.

Our cancer genetic, cell biological, and biophysical validation of the Lazy Piggy screen illustrate a clear mechanism in which potassium channels, particularly *KCNB2*, control intracellular potassium concentrations in SHH MB tumor cells. The absence of *KCNB2* dysregulates potassium efflux, leading to osmotic cell swelling and decreased membrane tension. This decrease in membrane tension facilitates the endocytosis of transmembrane proteins, such as EGFR, reducing EGFR signaling in SHH MPCs and causing tumor growth defects. These effects can be mimicked pharmacologically through manipulation of cell membrane tension, supporting our suggested model (Figure 6I). Our study links potassium channel function to the regulation of cell mechanics and mechano-chemical signaling in tumor-propagating cells, highlighting potassium homeostasis as a promising therapeutic target. *KCNB2* is non-essential in normal mouse development, thereby providing a favorable therapeutic window for targeted intervention.

Ion channels are highly druggable targets, due to their well-studied pharmacology and membrane localization. Indeed, ion channels are the second largest class membrane proteins (after G-protein-coupled receptors) as the targets of approved drugs.⁷⁷ While specific ion channels are overexpressed in cancer, their expression in non-malignant tissues is tightly regulated, providing a potential therapeutic window to target ion channels in cancer.^{38–40} Ions regulate the osmotic gradient across the plasma membrane, which in turn governs cell size and membrane tension. In this study, we establish a critical role of *KCNB2* in regulating the proliferation and mechanical properties of MPCs. It is noteworthy that MB is traditionally described as “small blue cell tumor” due to the small tumor cell volume and minimal cytoplasm.⁷⁸ Our results suggest that regulation of cell volume-gated plasma membrane tension plays a critical role in MB tumorigenesis. This indicates that the small cell volume observed in MB for over a century might be a

key factor in maintaining the malignant phenotype and presents a targetable biological phenomenon. Our study highlights the importance of cell volume homeostasis in MB, and future research to characterize the osmotic tumor microenvironment and to identify the regulators, sensors, and transducers of intracellular osmolarity may reveal further therapeutic opportunities.

Our previous studies showed that potassium channels *EAG2* and *KCNT2* and chloride channel *CLIC1* mediate potassium and chloride efflux required for pre-mitotic cytoplasmic condensation in rapidly dividing MB cells.^{79–81} This study of *KCNB2* in MB provided further insights into how ion channels regulate brain tumorigenesis. First, our prior studies focused on ion channel regulation of the highly proliferative cells that comprise the tumor bulk.^{80,81} Despite the importance of the rare, quiescent, and stem-like cells in cancer,⁸² it was unknown whether ion channels govern the pool of such tumor-propagating cells in MB. Second, our prior studies demonstrated that perturbing ion channel function impairs tumor cell proliferation by the P38 mitogen-activated protein kinase (MAPK) stress sensing pathway.^{79,81} However, it was unclear whether ion channels regulate oncogenic signaling by integrating cell volume homeostasis and cellular mechanics. Here, we demonstrate that *KCNB2* regulates MPC plasma membrane mechanics to govern pro-proliferative EGFR signaling.

In addition to the cell-autonomous functions of ion channels in cancer, previous studies in melanoma reported that necrotic tumor cells release intracellular ions into the extracellular fluid and tumor microenvironment.^{83,84} Elevated extracellular potassium impairs T cell effector function through ionic immune suppression, providing a link between extracellular ions, tumor-induced immune suppression, and immune-mediated tumor clearance.^{85,86} Thus, beyond cancer-cell-autonomous effects of ion channels, manipulating the ionic milieu of the tumor microenvironment by targeting ionic homeostasis may reveal additional strategies to augment cancer therapies.

Collectively, ion channels can regulate tumor growth by controlling cancer cell-intrinsic properties and how cancer cells interact with their microenvironment. Targeting ion channels and ionic homeostasis represent an exciting area to both understand the biology of cancer and develop mechanism-based treatment approaches.

Limitations of the study

We note several limitations of our study, including the small sample size of Lazy Piggy tumors, and the limited read depth captured for insertions in each tumor. This may explain why transcriptional upregulation and downregulation was not necessarily observed for putative gain- and loss-of-function maintenance insertions, respectively. A second limitation is that the restriction-splink PCR used to generate insertion libraries does not allow for direct estimation of insertion clonality as is the case with libraries

(F) Increased whole-cell expression of pEGFR signal in *SOX2⁺ Kcnb2^{+/+}* versus *Kcnb2^{-/-}* SHH MPCs.

(G) Increased whole-cell colocalization of pEGFR and Caveolin-1 in *SOX2⁺* SHH MPCs.

(H) Quantification of pEGFR signal in *SOX2⁺* SHH MPCs.

(I) Quantification of pEGFR and Caveolin-1 colocalization in *SOX2⁺* SHH MPCs indicates increased caveolar endocytosis of pEGFR in the absence of *Kcnb2*.

(J) Total internal reflection fluorescence (TIRF) microscopy quantification of the plasma membrane fractions of Caveolin-1 and pEGFR in *SOX2⁺* SHH MPCs. Increased Caveolin-1 and decreased pEGFR membrane fractions in the absence of *Kcnb2* suggest increased caveolar endocytosis and not a deficit in caveolar trafficking to the membrane.

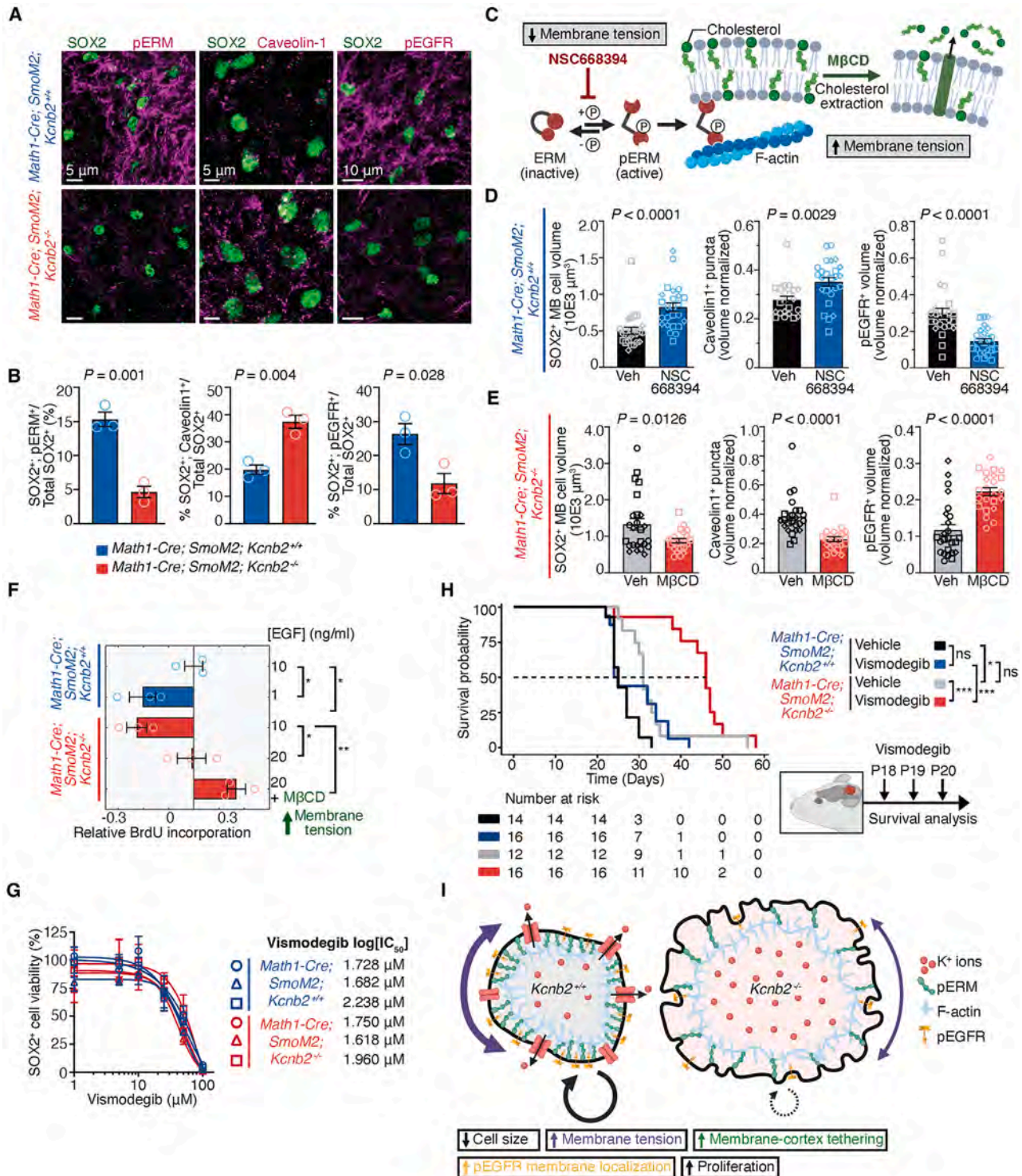


Figure 6. Ionic control of membrane tension and EGFR potentiate MB cell proliferation

(A and B) Representative immunohistochemistry (A) and quantification (B) of SOX2, pERM, Caveolin-1, and pEGFR, in P7 *Kcnb2^{+/+}* versus *Kcnb2^{-/-}* SHH MB. Loss of *Kcnb2* function *in vivo* results in decreased membrane tethering, increased Caveolin-1, and decreased pEGFR in SOX2⁺ MPCs. (C) Schematic of experiments to manipulate membrane tension. (Left) *Kcnb2^{+/+}* Sox2⁺ MPCs are treated with NSC668394, an inhibitor of ezrin phosphorylation, to reduce membrane tension. (Right) *Kcnb2^{-/-}* SOX2⁺ MPCs are treated with methyl-β-cyclodextrin (MβCD), which depletes cholesterol from the plasma membrane to increase membrane tension.

(legend continued on next page)

of varying fragment length produced with shear splink PCR. A third limitation is that the Lazy Piggy system enhances specificity but not sensitivity of existing insertional mutagenesis screens, and thus downstream validation of candidate genes and pathways remains a necessity. Further studies using the Lazy Piggy system would benefit from studying a larger cohort of animals to increase genomic coverage of transposon mobilization and remobilization to identify tumor maintenance drivers. A fourth limitation is that our mechanistic hypothesis about the anti-tumor effect of KCNB2 depletion assumes that reduced potassium efflux from MB cells will increase intracellular potassium concentrations, in turn driving osmotic cell swelling and membrane tension-gated changes in EGFR signaling. Although the transmembrane potassium gradient is universally conserved, we do not directly show that KCNB2 depletion increases intracellular potassium concentrations.

RESOURCE AVAILABILITY

Lead contact

Further information and requests for resources and reagents should be directed to and will be fulfilled by the lead contact, Xi Huang (xi.huang@sickkids.ca).

Materials availability

For all additional information and request for resources and reagents should be directed to and will be fulfilled by Dr. Xi Huang (xi.huang@sickkids.ca) and Dr. Michael D. Taylor (mdt.cns@gmail.com).

Data and code availability

Processed input data generated for this study and custom code used in the analyses are accessible on GitHub (https://github.com/anderswe/lazy_piggy) and Zenodo (<https://doi.org/10.5281/zenodo.14188406>). The restriction splink sequencing data (LP mouse tumours) and bulk RNAseq data (LP mouse tumours and *Math1-Cre*; *R26-LSL-SmoM2-eYFP* mouse tumours) generated in this study have been deposited in the Gene Expression Omnibus (GEO) database under the accessions [GSE277172](https://www.ncbi.nlm.nih.gov/geo/query/acc.cgi?acc=GSE277172) and [GSE277171](https://www.ncbi.nlm.nih.gov/geo/query/acc.cgi?acc=GSE277171), respectively. Any additional information required to reanalyze the data reported in this work paper is available from the [lead contact](#) upon request.

ACKNOWLEDGMENTS

This work is supported by Sontag Foundation Distinguished Scientist Award, Ontario Early Researcher Award, Canadian Cancer Society Challenge Grant, Cancer Research Society Operating Grant, Natural Sciences and Engineering Research Council Discovery Grant, American Brain Tumor Association Dis-

covery Grant, Ontario Institute for Cancer Research Translational Research Initiative, Canadian Institute of Health Research Project Grants, b.r.a.i.n.child, and Meagan's HUG to X.H. M.D.T. is supported by the NIH (R01NS106155, R01CA159859, and R01CA255369), The Pediatric Brain Tumour Foundation, The Terry Fox Research Institute, The Canadian Institutes of Health Research, The Cure Search Foundation, Matthew Larson Foundation (IronMatt), b.r.a.i.n.child, Meagan's Walk, SWIFTY Foundation, The Brain Tumour Charity, Genome Canada, Genome BC, Genome Quebec, the Ontario Research Fund, Worldwide Cancer Research, V-Foundation for Cancer Research, and the Ontario Institute for Cancer Research through funding provided by the Government of Ontario. M.D.T. is also supported by a Canadian Cancer Society Research Institute Impact grant, a Cancer Research UK Brain Tumour Award, and by a Stand Up To Cancer (SU2C) St. Baldrick's Pediatric Dream Team Translational Research Grant (SU2C-AACR-DT1113) and SU2C Canada Cancer Stem Cell Dream Team Research Funding (SU2C-AACR-DT-19-15) provided by the Government of Canada through Genome Canada and the Canadian Institutes of Health Research, with supplementary support from the Ontario Institute for Cancer Research through funding provided by the Government of Ontario. Stand Up to Cancer is a program of the Entertainment Industry Foundation administered by the American Association for Cancer Research. D.A.L. is supported by an American Cancer Society Research Professorship. J.J.F. is supported by Restracom Scholarship from The Hospital for Sick Children. Xian Wang is supported by Lap-Chee Tsui Fellowship from The Hospital for Sick Children and Dunn with Cancer Research Fellowship from Brain Tumour Foundation of Canada. A.W.E. is supported by Restracom Scholarship from The Hospital for Sick Children, the Canada Graduate Scholarship to Honour Nelson Mandela from the Canadian Institutes of Health Research and the Ruggles Innovation Award. J.C.-G. and X.C. are supported by Restracom Fellowship from The Hospital for Sick Children. S.B. is supported by International Postdoc Grant from Swedish Research Council. N.A. is supported by Childhood Cancer Research Postdoctoral Fellow Grant from Rally Foundation and Restracom Fellowship from The Hospital for Sick Children. We thank Paul Paroutis and Kimberly Lau at SickKids Imaging Facility for help with confocal imaging and image analysis. Schematics were created using BioRender. M.D.T. is a CPRIT Scholar in Cancer Research (CPRIT – RR220051) and the Cyvia and Melvyn Wolff Chair of Pediatric Neuro-Oncology, Texas Children's Cancer and Hematology Center. X.H. is a catalyst scholar at The Hospital for Sick Children and Canada Research Chair in Cancer Biophysics.

AUTHOR CONTRIBUTIONS

J.J.F. performed all mouse work and wet laboratory experiments. J.C.-G. performed functional validation experiments with the assistance from E.Y. for the revision of the manuscript. Xin Wang and Xiaochong Wu generated and performed validation experiments of the Lazy Piggy mouse. P.S. and A.W.E. performed bioinformatic analyses. Xian Wang performed membrane tension measurements. G.S. performed micropipette aspiration experiments. X.C. performed electrophysiology experiments and assisted with mouse work.

(D) Quantification of cell volume, Caveolin-1⁺ puncta, and pEGFR⁺ volume in *Kcnb2*^{+/+} SOX2⁺ MPCs treated with 25 μM NSC668394 (NSC) for 24 h *in vitro*. Pharmacologic inhibition of membrane tethering results in increased cell size, increased Caveolin-1, and decreased pEGFR, and phenocopies *Kcnb2* loss of function.

(E) Quantification of cell volume, Caveolin-1⁺ puncta, and pEGFR⁺ signal in *Kcnb2*^{-/-} SOX2⁺ MPCs treated with 1 mM MβCD for 24 h *in vitro*. Pharmacologic increase of membrane tension results in decreased cell size, decreased Caveolin-1, and increased pEGFR, phenocopies the *Kcnb2* wild-type condition.

(F) BrdU incorporation in SOX2⁺ MPCs after incubating for 3 h. Results are expressed as fold change relative to *Kcnb2*^{+/+} cells in standard culture conditions with 10 ng/mL EGF. Loss of *Kcnb2* function was associated with a similar proliferation deficit as with reduction in EGF supplementation, which was restored with augmented EGF concentration and enhanced with pharmacologic increase of membrane tension. "ns" denotes $p > 0.05$, * denotes $p \leq 0.05$, ** denotes $p \leq 0.01$, *** denotes $p \leq 0.001$, **** denotes $p \leq 0.0001$.

(G) *In vitro* dose-response experiments indicate that *Kcnb2* knockout does not sensitize MPCs to smoothened inhibition with vismodegib. Experiment was repeated using three biological replicates per genotype.

(H) Overall survival in *Kcnb2*^{+/+} versus *Kcnb2*^{-/-} mice predisposed to SHH MB (left) on 3-day treatment regimen with vismodegib or vehicle (right, schematic). Pharmacologic inhibition of hedgehog pathway in SHH MB cooperates with *Kcnb2* loss of function to prolong survival. "ns" denotes $p > 0.05$, * denotes $p \leq 0.05$, ** denotes $p \leq 0.01$, *** denotes $p \leq 0.001$, **** denotes $p \leq 0.0001$.

(I) Summary cartoon of biophysical mechanism of action for *Kcnb2* in MB. Overexpression of *Kcnb2* in SOX2⁺ MPCs drives increased K⁺ ion efflux, resulting in decreased cell size and increased actin-plasma membrane tethering and membrane tension. Increased membrane tension allows for plasma membrane retention of pEGFR by limiting caveolar endocytosis and is associated with increased cell proliferation.

Y.X., S.W., H.F., and A.S.M. assisted with bioinformatic analysis. S.B., M.A.F., R.J.P., and N.A. assisted with mouse work. All other authors contributed to methodology development and reagents. J.J.F. and A.W.E. wrote the manuscript with input from all other authors. X.H. and M.D.T. conceived and supervised the project.

DECLARATION OF INTERESTS

The authors declare no competing interests.

STAR★METHODS

Detailed methods are provided in the online version of this paper and include the following:

- KEY RESOURCES TABLE
- EXPERIMENTAL MODEL AND STUDY PARTICIPANT DETAILS
 - Mouse line generation
 - Human MB cell culture and experiments
- METHOD DETAILS
 - Lazy Piggy plasmid construction
 - *In vitro* validation of the Lazy Piggy system
 - Western blot analysis
 - Necropsy, tumor collection, and histological analysis
 - Histological analysis
 - Library preparation and sequencing
 - Lazy Piggy read processing, alignment and analysis
 - Bulk RNA-seq library preparation, data preprocessing, and analysis (Lazy Piggy tumors)
 - Bulk RNA-seq analysis (human MB and normal cerebellum)
 - Single cell RNA-seq analysis
 - Atomic force microscopy
 - Micropipette aspiration
- QUANTIFICATION AND STATISTICAL ANALYSIS

SUPPLEMENTAL INFORMATION

Supplemental information can be found online at <https://doi.org/10.1016/j.devcel.2025.01.001>.

Received: September 2, 2024

Revised: October 28, 2024

Accepted: January 3, 2025

Published: January 24, 2025

REFERENCES

1. Haber, D.A., and Settleman, J. (2007). Cancer: Drivers and passengers. *Nature* 446, 145–146. <https://doi.org/10.1038/446145a>.
2. Greenman, C., Stephens, P., Smith, R., Dalgleish, G.L., Hunter, C., Bignell, G., Davies, H., Teague, J., Butler, A., Stevens, C., et al. (2007). Patterns of somatic mutation in human cancer genomes. *Nature* 446, 153–158. <https://doi.org/10.1038/nature05610>.
3. Martínez-Jiménez, F., Muiños, F., Sentís, I., Deu-Pons, J., Reyes-Salazar, I., Arnedo-Pac, C., Mularoni, L., Pich, O., Bonet, J., Kranas, H., et al. (2020). A compendium of mutational cancer driver genes. *Nat. Rev. Cancer* 20, 555–572. <https://doi.org/10.1038/s41568-020-0290-x>.
4. Ostroverkhova, D., Przytycka, T.M., and Panchenko, A.R. (2023). Cancer driver mutations: predictions and reality. *Trends Mol. Med.* 29, 554–566. <https://doi.org/10.1016/j.molmed.2023.03.007>.
5. Gargiulo, G., Serresi, M., and Marine, J.-C. (2024). Cell states in cancer: drivers, passengers, and trailers. *Cancer Discov.* 14, 610–614. <https://doi.org/10.1158/2159-8290.CD-23-1510>.
6. Tokheim, C.J., Papadopoulos, N., Kinzler, K.W., Vogelstein, B., and Karchin, R. (2016). Evaluating the evaluation of cancer driver genes. *Proc. Natl. Acad. Sci. USA* 113, 14330–14335. <https://doi.org/10.1073/pnas.1616440113>.
7. Campbell, B.B., Light, N., Fabrizio, D., Zatzman, M., Fuligni, F., de Borja, R., Davidson, S., Edwards, M., Elvin, J.A., Hodel, K.P., et al. (2017). Comprehensive analysis of hypermutation in human cancer. *Cell* 171, 1042–1056.e10. <https://doi.org/10.1016/j.cell.2017.09.048>.
8. Wu, X., Northcott, P.A., Dubuc, A., Dupuy, A.J., Shih, D.J.H., Witt, H., Croul, S., Bouffet, E., Fults, D.W., Eberhart, C.G., et al. (2012). Clonal selection drives genetic divergence of metastatic medulloblastoma. *Nature* 482, 529–533. <https://doi.org/10.1038/nature10825>.
9. Yang, D., Jones, M.G., Naranjo, S., Rideout, W.M., Min, K.H. (Joseph), Ho, R., Wu, W., Replogle, J.M., Page, J.L., Quinn, J.J., et al. (2022). Lineage tracing reveals the phylogenetics, plasticity, and paths of tumor evolution. *Cell* 185, 1905–1923.e25. <https://doi.org/10.1016/j.cell.2022.04.015>.
10. Quinn, J.J., Jones, M.G., Okimoto, R.A., Nanjo, S., Chan, M.M., Yosef, N., Bivona, T.G., and Weissman, J.S. (2021). Single-cell lineages reveal the rates, routes, and drivers of metastasis in cancer xenografts. *Science* 371, eabc1944. <https://doi.org/10.1126/science.abc1944>.
11. Beckmann, P.J., Larson, J.D., Larsson, A.T., Ostergaard, J.P., Wagner, S., Rahrmann, E.P., Shamsan, G.A., Otto, G.M., Williams, R.L., Wang, J., et al. (2019). Sleeping beauty insertional mutagenesis reveals important genetic drivers of central nervous system embryonal tumors. *Cancer Res.* 79, 905–917. <https://doi.org/10.1158/0008-5472.CAN-18-1261>.
12. Dupuy, A.J., Akagi, K., Largaespada, D.A., Copeland, N.G., and Jenkins, N.A. (2005). Mammalian mutagenesis using a highly mobile somatic Sleeping Beauty transposon system. *Nature* 436, 221–226. <https://doi.org/10.1038/nature03691>.
13. Genovesi, L.A., Ng, C.G., Davis, M.J., Remke, M., Taylor, M.D., Adams, D.J., Rust, A.G., Ward, J.M., Ban, K.H., Jenkins, N.A., et al. (2013). Sleeping Beauty mutagenesis in a mouse medulloblastoma model defines networks that discriminate between human molecular subgroups. *Proc. Natl. Acad. Sci. USA* 110, E4325–E4334. <https://doi.org/10.1073/pnas.1318639110>.
14. Keng, V.W., Villanueva, A., Chiang, D.Y., Dupuy, A.J., Ryan, B.J., Matise, I., Silverstein, K.A.T., Sarver, A., Starr, T.K., Akagi, K., et al. (2009). A conditional transposon-based insertional mutagenesis screen for genes associated with mouse hepatocellular carcinoma. *Nat. Biotechnol.* 27, 264–274. <https://doi.org/10.1038/nbt.1526>.
15. Moriarity, B.S., Otto, G.M., Rahrmann, E.P., Rathe, S.K., Wolf, N.K., Weg, M.T., Manlove, L.A., LaRue, R.S., Temiz, N.A., Molyneux, S.D., et al. (2015). A Sleeping Beauty forward genetic screen identifies new genes and pathways driving osteosarcoma development and metastasis. *Nat. Genet.* 47, 615–624. <https://doi.org/10.1038/ng.3293>.
16. Morrissy, A.S., Garzia, L., Shih, D.J.H., Zuyderduyn, S., Huang, X., Skowron, P., Remke, M., Cavalli, F.M.G., Ramaswamy, V., Lindsay, P.E., et al. (2016). Divergent clonal selection dominates medulloblastoma at recurrence. *Nature* 529, 351–357. <https://doi.org/10.1038/nature16478>.
17. Rahrmann, E.P., Watson, A.L., Keng, V.W., Choi, K., Moriarity, B.S., Beckmann, D.A., Wolf, N.K., Sarver, A., Collins, M.H., Moertel, C.L., et al. (2013). Forward genetic screen for malignant peripheral nerve sheath tumor formation identifies new genes and pathways driving tumorigenesis. *Nat. Genet.* 45, 756–766. <https://doi.org/10.1038/ng.2641>.
18. Starr, T.K., Allaei, R., Silverstein, K.A.T., Staggs, R.A., Sarver, A.L., Bergemann, T.L., Gupta, M., O'Sullivan, M.G., Matise, I., Dupuy, A.J., et al. (2009). A transposon-based genetic screen in mice identifies genes altered in colorectal cancer. *Science* 323, 1747–1750. <https://doi.org/10.1126/science.1163040>.
19. Starr, T.K., Scott, P.M., Marsh, B.M., Zhao, L., Than, B.L.N., O'Sullivan, M.G., Sarver, A.L., Dupuy, A.J., Largaespada, D.A., and Cormier, R.T. (2011). A Sleeping Beauty transposon-mediated screen identifies murine susceptibility genes for adenomatous polyposis coli (Apc)-dependent intestinal tumorigenesis. *Proc. Natl. Acad. Sci. USA* 108, 5765–5770. <https://doi.org/10.1073/pnas.1018012108>.
20. Ostrom, Q.T., Cioffi, G., Waite, K., Kruchko, C., and Barnholtz-Sloan, J.S. (2021). CBTRUS statistical report: primary brain and other central nervous

- system tumors diagnosed in the United States in 2014–2018. *Neuro-Oncology* 23, iii1–iii105. <https://doi.org/10.1093/neuonc/noab200>.
21. Taylor, M.D., Northcott, P.A., Korshunov, A., Remke, M., Cho, Y.-J., Clifford, S.C., Eberhart, C.G., Parsons, D.W., Rutkowski, S., Gajjar, A., et al. (2012). Molecular subgroups of medulloblastoma: the current consensus. *Acta Neuropathol.* 123, 465–472. <https://doi.org/10.1007/s00401-011-0922-z>.
 22. Juraschka, K., and Taylor, M.D. (2019). Medulloblastoma in the age of molecular subgroups: a review. *J. Neurosurg. Pediatr.* 24, 353–363. <https://doi.org/10.3171/2019.5.PEDS18381>.
 23. Mulhern, R.K., Merchant, T.E., Gajjar, A., Reddick, W.E., and Kun, L.E. (2004). Late neurocognitive sequelae in survivors of brain tumours in childhood. *Lancet Oncol.* 5, 399–408. [https://doi.org/10.1016/S1470-2045\(04\)01507-4](https://doi.org/10.1016/S1470-2045(04)01507-4).
 24. Goodrich, L.V., Milenković, L., Higgins, K.M., and Scott, M.P. (1997). Altered Neural Cell Fates and Medulloblastoma in Mouse *patched* Mutants. *Science* 277, 1109–1113. <https://doi.org/10.1126/science.277.5329.1109>.
 25. Schüller, U., Heine, V.M., Mao, J., Kho, A.T., Dillon, A.K., Han, Y.-G., Huillard, E., Sun, T., Ligon, A.H., Qian, Y., et al. (2008). Acquisition of granule neuron precursor identity is a critical determinant of progenitor cell competence to form shh-induced medulloblastoma. *Cancer Cell* 14, 123–134. <https://doi.org/10.1016/j.ccr.2008.07.005>.
 26. Yang, Z.-J., Ellis, T., Markant, S.L., Read, T.-A., Kessler, J.D., Bourbonlous, M., Schüller, U., Machold, R., Fishell, G., Rowitch, D.H., et al. (2008). Medulloblastoma can be initiated by deletion of *patched* in lineage-restricted progenitors or stem cells. *Cancer Cell* 14, 135–145. <https://doi.org/10.1016/j.ccr.2008.07.003>.
 27. Mao, J., Ligon, K.L., Rakhlin, E.Y., Thayer, S.P., Bronson, R.T., Rowitch, D., and McMahon, A.P. (2006). A novel somatic mouse model to survey tumorigenic potential applied to the hedgehog pathway. *Cancer Res.* 66, 10171–10178. <https://doi.org/10.1158/0008-5472.CAN-06-0657>.
 28. Wu, X., Northcott, P.A., Croul, S., and Taylor, M.D. (2011). Mouse models of medulloblastoma. *Chin. J. Cancer* 30, 442–449. <https://doi.org/10.5732/cjc.011.10040>.
 29. Ding, S., Wu, X., Li, G., Han, M., Zhuang, Y., and Xu, T. (2005). Efficient transposition of the piggyBac (PB) transposon in mammalian cells and mice. *Cell* 122, 473–483. <https://doi.org/10.1016/j.cell.2005.07.013>.
 30. Largaespada, D.A., and Collier, L.S. (2008). Transposon-mediated mutagenesis in somatic cells. In *Chromosomal Mutagenesis*, G.D. Davis and K.J. Kayser, eds. (Humana Press), pp. 95–108. https://doi.org/10.1007/978-1-59745-232-8_7.
 31. Uren, A.G., Kool, J., Matentzoglou, K., Ridder, J. de, Mattison, J., Uitert, M. van, Lagcher, W., Sie, D., Tanger, E., Cox, T., et al. (2008). Large-scale mutagenesis in p19ARF- and p53-deficient mice identifies cancer genes and their collaborative networks. *Cell* 133, 727–741. <https://doi.org/10.1016/j.cell.2008.03.021>.
 32. Brett, B.T., Berquam-Vrieze, K.E., Nannapaneni, K., Huang, J., Scheetz, T.E., and Dupuy, A.J. (2011). Novel molecular and computational methods improve the accuracy of insertion site analysis in sleeping beauty-induced tumors. *PLoS One* 6, e24668. <https://doi.org/10.1371/journal.pone.0024668>.
 33. Tsherniak, A., Vazquez, F., Montgomery, P.G., Weir, B.A., Kryukov, G., Cowley, G.S., Gill, S., Harrington, W.F., Pantel, S., Krill-Burger, J.M., et al. (2017). Defining a cancer dependency map. *Cell* 170, 564–576.e16. <https://doi.org/10.1016/j.cell.2017.06.010>.
 34. Hendrikse, L.D., Haldipur, P., Saulnier, O., Millman, J., Sjoboen, A.H., Erickson, A.W., Ong, W., Gordon, V., Coudière-Morrison, L., Mercier, A.L., et al. (2022). Failure of human rhombic lip differentiation underlies medulloblastoma formation. *Nature* 609, 1021–1028. <https://doi.org/10.1038/s41586-022-05215-w>.
 35. Vladoiu, M.C., El-Hamamy, I., Donovan, L.K., Farooq, H., Holgado, B.L., Sundaravadanam, Y., Ramaswamy, V., Hendrikse, L.D., Kumar, S., Mack, S.C., et al. (2019). Childhood cerebellar tumours mirror conserved fetal transcriptional programs. *Nature* 572, 67–73. <https://doi.org/10.1038/s41586-019-1158-7>.
 36. Skowron, P., Farooq, H., Cavalli, F.M.G., Morrissy, A.S., Ly, M., Hendrikse, L.D., Wang, E.Y., Djambazian, H., Zhu, H., Mungall, K.L., et al. (2021). The transcriptional landscape of Shh medulloblastoma. *Nat. Commun.* 12, 1749. <https://doi.org/10.1038/s41467-021-21883-0>.
 37. Lonsdale, J., Thomas, J., Salvatore, M., Phillips, R., Lo, E., Shad, S., Hasz, R., Walters, G., Garcia, F., and Young, N. (2013). The Genotype-Tissue Expression (GTEx) project. *Nat. Genet.* 45, 580–585. <https://doi.org/10.1038/ng.2653>.
 38. Fan, J.J., and Huang, X. (2022). Ion channels in cancer: orchestrators of electrical signaling and cellular crosstalk. In *Reviews of Physiology, Biochemistry and Pharmacology*, 183 (Springer Berlin Heidelberg), pp. 103–133. https://doi.org/10.1007/112_2020_48.
 39. Huang, X., and Jan, L.Y. (2014). Targeting potassium channels in cancer. *J. Cell Biol.* 206, 151–162. <https://doi.org/10.1083/jcb.201404136>.
 40. Pardo, L.A., and Stühmer, W. (2014). The roles of K⁺ channels in cancer. *Nat. Rev. Cancer* 14, 39–48. <https://doi.org/10.1038/nrc3635>.
 41. Specca, D.J., Ogata, G., Mandikian, D., Bishop, H.I., Wiler, S.W., Eum, K., Wenzel, H.J., Doisy, E.T., Matt, L., Campi, K.L., et al. (2014). Deletion of the Kv2.1 delayed rectifier potassium channel leads to neuronal and behavioral hyperexcitability. *Genes Brain Behav.* 13, 394–408. <https://doi.org/10.1111/gbb.12120>.
 42. Thiffault, I., Specca, D.J., Austin, D.C., Cobb, M.M., Eum, K.S., Safina, N.P., Grote, L., Farrow, E.G., Miller, N., Soden, S., et al. (2015). A novel epileptic encephalopathy mutation in KCNB1 disrupts Kv2.1 ion selectivity, expression, and localization. *J. Gen. Physiol.* 146, 399–410. <https://doi.org/10.1085/jgp.201511444>.
 43. Torkamani, A., Bersell, K., Jorge, B.S., Bjork, R.L., Friedman, J.R., Bloss, C.S., Cohen, J., Gupta, S., Naidu, S., Vanoye, C.G., et al. (2014). De novo KCNB1 mutations in epileptic encephalopathy. *Ann. Neurol.* 76, 529–540. <https://doi.org/10.1002/ana.24263>.
 44. de Kovel, C.G.F., Syrbe, S., Brilstra, E.H., Verbeek, N., Kerr, B., Dubbs, H., Bayat, A., Desai, S., Naidu, S., Srivastava, S., et al. (2017). Neurodevelopmental disorders caused by de novo variants in KCNB1 genotypes and phenotypes. *JAMA Neurol.* 74, 1228–1236. <https://doi.org/10.1001/jamaneurol.2017.1714>.
 45. Sanguinetti, M.C., and Tristani-Firouzi, M. (2006). hERG potassium channels and cardiac arrhythmia. *Nature* 440, 463–469. <https://doi.org/10.1038/nature04710>.
 46. Groza, T., Gomez, F.L., Mashhadi, H.H., Muñoz-Fuentes, V., Gunes, O., Wilson, R., Cacheiro, P., Frost, A., Keskivai-Bond, P., Vardal, B., et al. (2023). The International Mouse Phenotyping Consortium: comprehensive knockout phenotyping underpinning the study of human disease. *Nucleic Acids Res.* 51, D1038–D1045. <https://doi.org/10.1093/nar/gkac972>.
 47. Dickinson, M.E., Flenniken, A.M., Ji, X., Teboul, L., Wong, M.D., White, J.K., Meehan, T.F., Wengler, W.J., Westerberg, H., Adissu, H., et al. (2016). High-throughput discovery of novel developmental phenotypes. *Nature* 537, 508–514. <https://doi.org/10.1038/nature19356>.
 48. Bhat, S., Rousseau, J., Michaud, C., Lourenço, C.M., Stoler, J.M., Louie, R.J., Clarkson, L.K., Lichty, A., Koboldt, D.C., Reshmi, S.C., et al. (2024). Mono-allelic *KCNB2* variants lead to a neurodevelopmental syndrome caused by altered channel inactivation. *Am. J. Hum. Genet.* 111, 761–777. <https://doi.org/10.1016/j.ajhg.2024.02.014>.
 49. Bar, C., Barcia, G., Jennesson, M., Le Guyader, G., Schneider, A., Mignot, C., Lesca, G., Breuillard, D., Montomoli, M., Keren, B., et al. (2020). Expanding the genetic and phenotypic relevance of *KCNB1* variants in developmental and epileptic encephalopathies: 27 new patients and overview of the literature. *Hum. Mutat.* 41, 69–80. <https://doi.org/10.1002/humu.23915>.
 50. Vanner, R.J., Remke, M., Gallo, M., Selvadurai, H.J., Coutinho, F., Lee, L., Kushida, M., Head, R., Morrissy, S., Zhu, X., et al. (2014). Quiescent Sox2⁺ cells drive hierarchical growth and relapse in sonic hedgehog

- subgroup medulloblastoma. *Cancer Cell* 26, 33–47. <https://doi.org/10.1016/j.ccr.2014.05.005>.
51. Zhang, L., He, X., Liu, X., Zhang, F., Huang, L.F., Potter, A.S., Xu, L., Zhou, W., Zheng, T., Luo, Z., et al. (2019). Single-cell transcriptomics in medulloblastoma reveals tumor-initiating progenitors and oncogenic cascades during tumorigenesis and relapse. *Cancer Cell* 36, 302–318.e7. <https://doi.org/10.1016/j.ccell.2019.07.009>.
52. Hovestadt, V., Smith, K.S., Bihannic, L., Filbin, M.G., Shaw, M.L., Baumgartner, A., DeWitt, J.C., Groves, A., Mayr, L., Weisman, H.R., et al. (2019). Resolving medulloblastoma cellular architecture by single-cell genomics. *Nature* 572, 74–79. <https://doi.org/10.1038/s41586-019-1434-6>.
53. Riemondy, K.A., Venkataraman, S., Willard, N., Nellan, A., Sanford, B., Griesinger, A.M., Amani, V., Mitra, S., Hankinson, T.C., Handler, M.H., et al. (2022). Neoplastic and immune single-cell transcriptomics define subgroup-specific intra-tumoral heterogeneity of childhood medulloblastoma. *Neuro-Oncology* 24, 273–286. <https://doi.org/10.1093/neuro-onc/noab135>.
54. Chen, X., Momin, A., Wanggou, S., Wang, X., Min, H.-K., Dou, W., Gong, Z., Chan, J., Dong, W., Fan, J.J., et al. (2023). Mechanosensitive brain tumor cells construct blood-tumor barrier to mask chemosensitivity. *Neuron* 111, 30–48.e14. <https://doi.org/10.1016/j.neuron.2022.10.007>.
55. Huang, X., Ketova, T., Litingtung, Y., and Chiang, C. (2010). Isolation, enrichment, and maintenance of medulloblastoma stem cells. *J. Vis. Exp.* 2086. <https://doi.org/10.3791/2086>.
56. Hille, B. (2001). *Ion Channels of Excitable Membranes, Third Edition* (Sinauer Associates is an imprint of Oxford University Press).
57. Dai, J., Sheetz, M.P., Wan, X., and Morris, C.E. (1998). Membrane tension in swelling and shrinking molluscan neurons. *J. Neurosci.* 18, 6681–6692. <https://doi.org/10.1523/JNEUROSCI.18-17-06681.1998>.
58. Pietuch, A., Brückner, B.R., and Janshoff, A. (2013). Membrane tension homeostasis of epithelial cells through surface area regulation in response to osmotic stress. *Biochim. Biophys. Acta* 1833, 712–722. <https://doi.org/10.1016/j.bbamcr.2012.11.006>.
59. Roffay, C., Molinard, G., Kim, K., Urbanska, M., Andrade, V., Barbarasa, V., Nowak, P., Mercier, V., García-Calvo, J., Matile, S., et al. (2021). Passive coupling of membrane tension and cell volume during active response of cells to osmosis. *Proc. Natl. Acad. Sci. USA* 118, e2103228118. <https://doi.org/10.1073/pnas.2103228118>.
60. Fehon, R.G., McClatchey, A.I., and Bretscher, A. (2010). Organizing the cell cortex: the role of ERM proteins. *Nat. Rev. Mol. Cell Biol.* 11, 276–287. <https://doi.org/10.1038/nrm2866>.
61. Raucher, D., and Sheetz, M.P. (1999). Membrane expansion increases endocytosis rate during mitosis. *J. Cell Biol.* 144, 497–506. <https://doi.org/10.1083/jcb.144.3.497>.
62. Dai, J., and Sheetz, M.P. (1995). Regulation of endocytosis, exocytosis, and shape by membrane tension. *Cold Spring Harb. Symp. Quant. Biol.* 60, 567–571. <https://doi.org/10.1101/SQB.1995.060.01.060>.
63. De Belly, H., Stubb, A., Yanagida, A., Labouesse, C., Jones, P.H., Paluch, E.K., and Chalut, K.J. (2021). Membrane tension gates ERK-mediated regulation of pluripotent cell fate. *Cell Stem Cell* 28, 273–284.e6. <https://doi.org/10.1016/j.stem.2020.10.018>.
64. Thottacherry, J.J., Kosmalska, A.J., Kumar, A., Vishen, A.S., Elosegui-Artola, A., Pradhan, S., Sharma, S., Singh, P.P., Guadamillas, M.C., Chaudhary, N., et al. (2018). Mechanochemical feedback control of dynamin independent endocytosis modulates membrane tension in adherent cells. *Nat. Commun.* 9, 4217. <https://doi.org/10.1038/s41467-018-06738-5>.
65. Sigismund, S., Lanzetti, L., Scita, G., and Di Fiore, P.P. (2021). Endocytosis in the context-dependent regulation of individual and collective cell properties. *Nat. Rev. Mol. Cell Biol.* 22, 625–643. <https://doi.org/10.1038/s41580-021-00375-5>.
66. Pollard, S.M., Yoshikawa, K., Clarke, I.D., Danovi, D., Stricker, S., Russell, R., Bayani, J., Head, R., Lee, M., Bernstein, M., et al. (2009). Glioma stem cell lines expanded in adherent culture have tumor-specific phenotypes and are suitable for chemical and genetic screens. *Cell Stem Cell* 4, 568–580. <https://doi.org/10.1016/j.stem.2009.03.014>.
67. Bulut, G., Hong, S.H., Chen, K., Beauchamp, E.M., Rahim, S., Kosturko, G.W., Glasgow, E., Dakshanamurthy, S., Lee, H.S., Daar, I., et al. (2012). Small molecule inhibitors of ezrin inhibit the invasive phenotype of osteosarcoma cells. *Oncogene* 31, 269–281. <https://doi.org/10.1038/onc.2011.245>.
68. Biswas, A., Kashyap, P., Datta, S., SenGupta, T., and Sinha, B. (2019). Cholesterol depletion by M β CD enhances cell membrane tension and its variations-reducing integrity. *Biophys. J.* 116, 1456–1468. <https://doi.org/10.1016/j.bpj.2019.03.016>.
69. Rodal, S.K., Skretting, G., Garred, O., Vilhardt, F., van Deurs, B., and Sandvig, K. (1999). Extraction of cholesterol with methyl- β -cyclodextrin perturbs formation of clathrin-coated endocytic vesicles. *Mol. Biol. Cell* 10, 961–974.
70. Li, Y., Song, Q., and Day, B.W. (2019). Phase I and phase II sonidegib and vismodegib clinical trials for the treatment of paediatric and adult MB patients: a systemic review and meta-analysis. *Acta Neuropathol. Commun.* 7, 123. <https://doi.org/10.1186/s40478-019-0773-8>.
71. Ocasio, J.K., Babcock, B., Malawsky, D., Weir, S.J., Loo, L., Simon, J.M., Zylka, M.J., Hwang, D., Dismuke, T., Sokolsky, M., et al. (2019). scRNA-seq in medulloblastoma shows cellular heterogeneity and lineage expansion support resistance to SHH inhibitor therapy. *Nat. Commun.* 10, 5829. <https://doi.org/10.1038/s41467-019-13657-6>.
72. Takeda, H., Jenkins, N.A., and Copeland, N.G. (2021). Identification of cancer driver genes using Sleeping Beauty transposon mutagenesis. *Cancer Sci.* 112, 2089–2096. <https://doi.org/10.1111/cas.14901>.
73. Yuan, W., Wu, S., Guo, J., Chen, Z., Ge, J., Yang, P., Hu, B., and Chen, Z. (2010). Silencing of TKTL1 by siRNA inhibits proliferation of human gastric cancer cells in vitro and in vivo. *Cancer Biol. Ther.* 9, 710–716. <https://doi.org/10.4161/cbt.9.9.11431>.
74. Diaz-Moralli, S., Aguilar, E., Marin, S., Coy, J.F., Dewerchin, M., Antoniewicz, M.R., Meca-Cortés, O., Notebaert, L., Ghesquière, B., Eelen, G., et al. (2016). A key role for transketolase-like 1 in tumor metabolic reprogramming. *Oncotarget* 7, 51875–51897. <https://doi.org/10.18632/oncotarget.10429>.
75. Pinson, A., Xing, L., Namba, T., Kalebic, N., Peters, J., Oegema, C.E., Traikov, S., Reppe, K., Riesenberger, S., Maricic, T., et al. (2022). Human TKTL1 implies greater neurogenesis in frontal neocortex of modern humans than Neanderthals. *Science* 377, eab16422. <https://doi.org/10.1126/science.ab16422>.
76. Kinnersley, B., Sud, A., Everall, A., Cornish, A.J., Chubb, D., Culliford, R., Gruber, A.J., Lärkeryd, A., Mitsopoulos, C., Wedge, D., et al. (2024). Analysis of 10,478 cancer genomes identifies candidate driver genes and opportunities for precision oncology. *Nat. Genet.* 56, 1868–1877. <https://doi.org/10.1038/s41588-024-01785-9>.
77. Santos, R., Ursu, O., Gaulton, A., Bento, A.P., Donadi, R.S., Bologa, C.G., Karlsson, A., Al-Lazikani, B., Hersey, A., Oprea, T.I., et al. (2017). A comprehensive map of molecular drug targets. *Nat. Rev. Drug Discov.* 16, 19–34. <https://doi.org/10.1038/nrd.2016.230>.
78. Bailey, P., and Cushing, H. (1925). Medulloblastoma cerebelli: a common type of midcerebellar glioma of childhood. *Arch. Neuropsych.* 14, 192–224. <https://doi.org/10.1001/archneuropsych.1925.02200140055002>.
79. Huang, X., Dubuc, A.M., Hashizume, R., Berg, J., He, Y., Wang, J., Chiang, C., Cooper, M.K., Northcott, P.A., Taylor, M.D., et al. (2012). Voltage-gated potassium channel EAG2 controls mitotic entry and tumor growth in medulloblastoma via regulating cell volume dynamics. *Genes Dev.* 26, 1780–1796. <https://doi.org/10.1101/gad.193789.112>.
80. Huang, X., He, Y., Dubuc, A.M., Hashizume, R., Zhang, W., Reimand, J., Yang, H., Wang, T.A., Stehbins, S.J., Younger, S., et al. (2015). EAG2 potassium channel with evolutionarily conserved function as a brain tumor target. *Nat. Neurosci.* 18, 1236–1246. <https://doi.org/10.1038/nn.4088>.
81. Francisco, M.A., Wanggou, S., Fan, J.J., Dong, W., Chen, X., Momin, A., Abeyundara, N., Min, H.-K., Chan, J., McAdam, R., et al. (2020). Chloride

- intracellular channel 1 cooperates with potassium channel EAG2 to promote medulloblastoma growth. *J. Exp. Med.* 217, e20190971. <https://doi.org/10.1084/jem.20190971>.
82. Kreso, A., and Dick, J.E. (2014). Evolution of the cancer stem cell model. *Cell Stem Cell* 14, 275–291. <https://doi.org/10.1016/j.stem.2014.02.006>.
83. Eil, R., Vodnala, S.K., Clever, D., Klebanoff, C.A., Sukumar, M., Pan, J.H., Palmer, D.C., Gros, A., Yamamoto, T.N., Patel, S.J., et al. (2016). Ionic immune suppression within the tumour microenvironment limits T cell effector function. *Nature* 537, 539–543. <https://doi.org/10.1038/nature19364>.
84. Vodnala, S.K., Eil, R., Kishton, R.J., Sukumar, M., Yamamoto, T.N., Ha, N.-H., Lee, P.-H., Shin, M., Patel, S.J., Yu, Z., et al. (2019). T cell stemness and dysfunction in tumors are triggered by a common mechanism. *Science* 363, eaau0135. <https://doi.org/10.1126/science.aau0135>.
85. Chandy, K.G., and Norton, R.S. (2016). Immunology: Channelling potassium to fight cancer. *Nature* 537, 497–499. <https://doi.org/10.1038/nature19467>.
86. Baixauli, F., Villa, M., and Pearce, E.L. (2019). Potassium shapes anti-tumor immunity. *Science* 363, 1395–1396. <https://doi.org/10.1126/science.aaw8800>.
87. Mátés, L., Chuah, M.K.L., Belay, E., Jerchow, B., Manoj, N., Acosta-Sanchez, A., Grzela, D.P., Schmitt, A., Becker, K., Matrai, J., et al. (2009). Molecular evolution of a novel hyperactive Sleeping Beauty transposase enables robust stable gene transfer in vertebrates. *Nat. Genet.* 41, 753–761. <https://doi.org/10.1038/ng.343>.
88. Kawaguchi, A., Miyata, T., Sawamoto, K., Takashita, N., Murayama, A., Akamatsu, W., Ogawa, M., Okabe, M., Tano, Y., Goldman, S.A., et al. (2001). Nestin-EGFP transgenic mice: visualization of the self-renewal and multipotency of CNS stem cells. *Mol. Cell. Neurosci.* 17, 259–273. <https://doi.org/10.1006/mcne.2000.0925>.
89. Li, M.A., Pettitt, S.J., Eckert, S., Ning, Z., Rice, S., Cadiñanos, J., Yusa, K., Conte, N., and Bradley, A. (2013). The piggyBac transposon displays local and distant reintegration preferences and can cause mutations at noncanonical integration sites. *Mol. Cell. Biol.* 33, 1317–1330. <https://doi.org/10.1128/MCB.00670-12>.
90. A. Nagy, ed. (2003). *Manipulating the Mouse Embryo: a Laboratory Manual, Third Edition* (Cold Spring Harbor Laboratory Press).
91. Joshi, M., Keith Pittman, H., Haisch, C., and Verbanac, K. (2008). Real-time PCR to determine transgene copy number and to quantitate the bio-localization of adoptively transferred cells from EGFP-transgenic mice. *BioTechniques* 45, 247–258. <https://doi.org/10.2144/000112913>.
92. Matei, V., Pauley, S., Kaing, S., Rowitch, D., Beisel, K.W., Morris, K., Feng, F., Jones, K., Lee, J., and Fritzsche, B. (2005). Smaller inner ear sensory epithelia in Neurog 1 null mice are related to earlier hair cell cycle exit. *Dev. Dyn.* 234, 633–650. <https://doi.org/10.1002/dvdy.20551>.
93. Jeong, J., Mao, J., Tenzen, T., Kottmann, A.H., and McMahon, A.P. (2004). Hedgehog signaling in the neural crest cells regulates the patterning and growth of facial primordia. *Genes Dev.* 18, 937–951. <https://doi.org/10.1101/gad.1190304>.
94. Hermansteyne, T.O., Kihira, Y., Misono, K., Deitchler, A., Yanagawa, Y., and Misonou, H. (2010). Immunolocalization of the voltage-gated potassium channel Kv2.2 in GABAergic neurons in the basal forebrain of rats and mice. *J. Comp. Neurol.* 518, 4298–4310. <https://doi.org/10.1002/cne.22457>.
95. Tronche, F., Kellendonk, C., Kretz, O., Gass, P., Anlag, K., Orban, P.C., Bock, R., Klein, R., and Schütz, G. (1999). Disruption of the glucocorticoid receptor gene in the nervous system results in reduced anxiety. *Nat. Genet.* 23, 99–103. <https://doi.org/10.1038/12703>.
96. Cadiñanos, J., and Bradley, A. (2007). Generation of an inducible and optimized piggyBac transposon system. *Nucleic Acids Res.* 35, e87. <https://doi.org/10.1093/nar/gkm446>.
97. Largaespada, D.A., and Collier, L.S. (2008). Transposon-mediated mutagenesis in somatic cells: identification of transposon-genomic DNA junctions. *Methods Mol. Biol.* 435, 95–108. https://doi.org/10.1007/978-1-59745-232-8_7.
98. Uren, A.G., Mikkers, H., Kool, J., van der Weyden, L., Lund, A.H., Wilson, C.H., Rance, R., Jonkers, J., van Lohuizen, M., Berns, A., et al. (2009). A high-throughput splinkerette-PCR method for the isolation and sequencing of retroviral insertion sites. *Nat. Protoc.* 4, 789–798. <https://doi.org/10.1038/nprot.2009.64>.
99. Schachter, N.F., Adams, J.R., Skowron, P., Kozma, K.J., Lee, C.A., Raghuram, N., Yang, J., Loch, A.J., Wang, W., Kucharczuk, A., et al. (2021). Single allele loss-of-function mutations select and sculpt conditional cooperative networks in breast cancer. *Nat. Commun.* 12, 5238. <https://doi.org/10.1038/s41467-021-25467-w>.
100. Temiz, N.A., Moriarity, B.S., Wolf, N.K., Riordan, J.D., Dupuy, A.J., Largaespada, D.A., and Sarver, A.L. (2016). RNA sequencing of Sleeping Beauty transposon-induced tumors detects transposon-RNA fusions in forward genetic cancer screens. *Genome Res.* 26, 119–129. <https://doi.org/10.1101/gr.188649.114>.
101. Dobin, A., Davis, C.A., Schlesinger, F., Drenkow, J., Zaleski, C., Jha, S., Batut, P., Chaisson, M., and Gingeras, T.R. (2013). STAR: ultrafast universal RNA-seq aligner. *Bioinformatics* 29, 15–21. <https://doi.org/10.1093/bioinformatics/bts635>.
102. Love, M.I., Huber, W., and Anders, S. (2014). Moderated estimation of fold change and dispersion for RNA-seq data with DESeq2. *Genome Biol.* 15, 550. <https://doi.org/10.1186/s13059-014-0550-8>.
103. McInnes, L., Healy, J., and Melville, J. (2020). UMAP: uniform manifold approximation and projection for dimension reduction. Preprint at arXiv. <https://doi.org/10.48550/arXiv.1802.03426>.
104. Chen, X., Wanggou, S., Bodalia, A., Zhu, M., Dong, W., Fan, J.J., Yin, W.C., Min, H.-K., Hu, M., Draghici, D., et al. (2018). A feedforward mechanism mediated by mechanosensitive ion channel PIEZO1 and tissue mechanics promotes glioma aggression. *Neuron* 100, 799–815. <https://doi.org/10.1016/j.neuron.2018.09.046>.
105. Pietuch, A., and Janshoff, A. (2013). Mechanics of spreading cells probed by atomic force microscopy. *Open Biol.* 3, 130084. <https://doi.org/10.1098/rsob.130084>.
106. Wang, X., Liu, H., Zhu, M., Cao, C., Xu, Z., Tsatskis, Y., Lau, K., Kuok, C., Filleter, T., McNeill, H., et al. (2018). Mechanical stability of the cell nucleus – roles played by the cytoskeleton in nuclear deformation and strain recovery. *J. Cell Sci.* 131, jcs209627. <https://doi.org/10.1242/jcs.209627>.
107. Therneau, T.M., and Grambsch, P.M. (2000). *Modeling Survival Data: Extending the Cox Model* (Springer).
108. R Core Team (2022). *R: A Language and Environment for Statistical Computing* (R Foundation for Statistical Computing).
109. Hao, Y., Hao, S., Andersen-Nissen, E., Mauck, W.M., Zheng, S., Butler, A., Lee, M.J., Wilk, A.J., Darby, C., Zager, M., et al. (2021). Integrated analysis of multimodal single-cell data. *Cell* 184, 3573–3587. <https://doi.org/10.1016/j.cell.2021.04.048>.
110. Korsunsky, I., Millard, N., Fan, J., Slowikowski, K., Zhang, F., Wei, K., Baglaenko, Y., Brenner, M., Loh, P.R., and Raychaudhuri, S. (2019). Fast, sensitive and accurate integration of single-cell data with Harmony. *Nat. Methods* 16, 1289–1296. <https://doi.org/10.1038/s41592-019-0619-0>.

STAR★METHODS

KEY RESOURCES TABLE

REAGENT or RESOURCE	SOURCE	IDENTIFIER
Antibodies		
Chicken anti-GFP	Antibodies Incorporated	Cat# GFP-1020; RRID:AB_10000240
Mouse anti-alpha-Tubulin	Sigma-Aldrich	Cat# T6199; RRID:AB_477583
Mouse anti-BrdU (G3G4)	DSHB	Cat# G3G4; RRID:AB_2618097
Mouse anti-Caveolin-1 (7C8)	Novus	Cat# NB100-615;RRID:AB_10003431
Mouse anti-KCNB2 (N372B/1)	NeuroMab	Cat# 75-369; RRID: AB_2315870
Mouse anti-PCNA (PC10)	Santa Cruz Biotechnology	Cat# sc-56; RRID:AB_628110
Mouse anti-SOX2	abcam	Cat# ab79351; RRID:AB_10710406
Rabbit anti-Caveolin-1 (D46G3)	Cell Signaling Technology	Cat# 3267; RRID:AB_2275453
Rabbit anti-Clathrin Heavy Chain (D3C6)	Cell Signaling Technology	Cat# 4796; RRID:AB_10828486
Rabbit anti-DCX	abcam	Cat# ab18723; RRID:AB_732011
Rabbit anti-Ki67	abcam	Cat# ab15580; RRID:AB_443209
Rabbit anti-NeuN	abcam	Cat# ab104225;RRID:AB_10711153
Rabbit anti-pEGFR (Y1068)	Cell Signaling Technology	Cat# 3777; RRID:AB_2096270
Rabbit anti-pEGFR (Y1068)	abcam	Cat# ab40815; RRID:AB_732110
Rabbit anti-pERK1/2	Cell Signaling Technology	Cat# 4370; RRID:AB_2315112
Rabbit anti-Phospho-Ezrin/Radixin/Moesin	Cell Signaling Technology	Cat# 3726; RRID:AB_10560513
Rabbit anti-Rab5	Cell Signaling Technology	Cat# 3547; RRID:AB_2300649
Rabbit anti-SOX2	abcam	Cat# ab97959; RRID:AB_2341193
Rat anti-BrdU	abcam	Cat# ab6326; RRID:AB_305426
Rat anti-Ki67 (SolA15)	Ebioscience	Cat# 14-5698-82;RRID:AB_10854564
Mouse anti-ER α	Santa Cruz Biotechnology	Cat # Sc-56833
Mouse anti-hemagglutinin	Abcam	Cat # ab49969; RRID: AB_880330
Chemicals, peptides, and recombinant proteins		
DAPI	Sigma-Aldrich	Cat# D9564
Alexa Fluor 488 Phalloidin	Invitrogen	Cat# A12379; RRID: AB_2315147
4-Aminopyridine	TOCRIS	Cat# 0940
Accutase	Stem Cell Technologies	Cat# 07920
BrdU	Roche	Cat# 10280879001
Distilled water	Gibco	Cat# 15230147
Vismodegib (GDC-0449)	Selleck Chemicals	Cat# S1082
Human recombinant EGF	StemCell Technologies	Cat# 78006
Human TGF- α recombinant protein	Gibco	Cat# PHG0051
Laminin	Sigma-Aldrich	Cat# L2020
Methyl- β -cyclodextrin	Santa Cruz Biotechnology	Cat# sc-215379A
NeuroCult NS-ABasal Medium (Mouse)	StemCell Technologies	Cat# 05750
NSC668394	Sigma-Aldrich	Cat# 341216
Poly-L-ornithine	Sigma-Aldrich	Cat # P4957
Polyethylene Glycol 1500	Sigma-Aldrich	Cat # 10783641001
Recombinant Human Amphiregulin Protein	R&D Systems	Cat # 262-AR-100/CF
4-Hydroxytamoxifen	Sigma	Cat# T5648
DMEM	Thermo Fisher	Cat# 11995073
FBS	Thermo Fisher	Cat# 12483020
Lipofectamine 3000	Thermo Fisher	Cat# L3000001

(Continued on next page)

Continued

REAGENT or RESOURCE	SOURCE	IDENTIFIER
Critical commercial assays		
Apoptag Fluorescein In Situ Apoptosis Detection Kit	Millipore	Cat# 7110
Proteome Profiler Phospho-RTK Array Kit	Bio-technie	Catalog # ARY014
Deposited data		
SHH MB scRNA-seq normalized counts	Hovestadt et al., ⁵² Riemondy et al. ⁵³	GEO: GSE119926 and GSE155446
SHH MB RNA-seq	Hendrikse et al., ³⁴ Vladoiu et al., ³⁵ Skowron et al. ³⁶	EGA: EGAD00001004435 and EGAS00001005826 and EGAD00001006305
SHH MB and Lazy Piggy mouse tumor DNA-seq and RNA-seq	This paper	GEO: GSE277171 and GSE277172
Normal cerebellum bulk RNA-seq	Lonsdale et al. ³⁷	phs000424.v6.p1
Experimental models: Cell lines		
Mouse SOX2 ⁺ MB cells	This paper	N/A
ONS76 cell line	Laboratory of Dr. Michael D. Taylor, Baylor College of Medicine	N/A
Experimental models: Organisms/strains		
<i>Ptch1</i> ^{+/-}	The Jackson Laboratory	RRID:IMSR_JAX:003081
<i>Math1-Cre</i>	The Jackson Laboratory	RRID:IMSR_JAX:011104
<i>Rosa26-LSL-SmoM2-YFP</i>	The Jackson Laboratory	RRID:IMSR_JAX:005130
<i>Nestin-Cre</i>	The Jackson Laboratory	RRID:IMSR_JAX:003771
<i>Kcnc2</i> ^{tm1Lex}	European Mouse Mutant Archive	EM:02354
<i>Rosa26-LSL-mPB-L3-ERT2</i>	Laboratory of Dr. Allen Bradley, Wellcome Trust Sanger Institute	N/A
<i>Lazy Piggy</i> (Founder #129; 1000+ copies chr7)	This paper	N/A
<i>Lazy Piggy</i> (Founder #137; 600+ copies chr10)	This paper	N/A
Oligonucleotides		
Primers for <i>Lazy Piggy</i> library preparation and sequencing, see Table S1	This paper	N/A
hKCNB1 RT-qPCR primers: 5'-CTGTCTGAAACCAGCTCAAG-3'; 5'-GTCTTCCAACCTGCTGAACG-3'	This paper	N/A
hKCNH2 RT-qPCR primers: 5'-CAACCTGGGCGACCAGATAG-3'; 5'-GGTGTTGGGAGAGACGTTGC-3'	This paper	N/A
hSMARCA4 RT-qPCR primers: 5'-AGTGCTGCTGTTCTGCCAAAT-3'; 5'-GGCTCGTTGAAGGTTTTTCAG-3'	This paper	N/A
hDYNC1H1 RT-qPCR primers: 5'-GCCACCGTCAGTTTTGACAC-3'; 5'-AAATTGCCTCCACCAAACGC-3'	This paper	N/A
hAHCYL RT-qPCR primers: 5'-CCTGCGTAAAGGTGGTATGT-3'; 5'-GAGTGGAGGAAGGGCTATACTA-3'	This paper	N/A
Recombinant DNA		
Plasmid: pcDNA 6.2 N-emGFP	Invitrogen	Cat # V35620
Plasmid: pcDNA3.1 ⁺ -KCNB2 cDNA	GenScript	Clone ID: OHu25595
<i>Lazy Piggy</i> transposon	This paper	https://github.com/anderswe/lazy_piggy/tree/main/transposon_vector
Software and algorithms		
GraphPad Prism 9	GraphPad Software, Inc.	https://www.graphpad.com/scientific-software/prism/
Imaris 9.3	Oxford Instruments	https://imaris.oxinst.com/versions/9-3

(Continued on next page)

Continued

REAGENT or RESOURCE	SOURCE	IDENTIFIER
STAR (2.5.4b)	Dobin et al. ¹⁰¹	https://github.com/alexdobin/STAR
R programming language (4.1.3)	R Core Team ¹⁰⁸	https://www.R-project.org/
{DESeq2} (1.34.0)	Love et al. ¹⁰²	https://bioconductor.org/packages/release/bioc/html/DESeq2.html
{umap} (0.2.8.0)	McInnes et al. ¹⁰³	https://github.com/tkonopka/umap
{survival} (3.3-1)	Therneau and Grambsch ¹⁰⁷	https://CRAN.R-project.org/package=survival
{Seurat} (4.1.0)	Hao et al. ¹⁰⁹	https://satijalab.org/seurat/
{harmony} (0.1.0)	Korsunsky et al. ¹¹⁰	https://github.com/immunogenomics/

EXPERIMENTAL MODEL AND STUDY PARTICIPANT DETAILS

Mouse line generation

Nestin-Cre transgenic mice obtained from Jackson Laboratories (JAX stock #003771). To generate *Nestin:Luc-SB100* transgenic mice, SB100 cDNA was excised from the vector pCMV-SB100,⁸⁷ luciferase-tagged, then inserted into nes1852tk/lacZ plasmid, which carried the Nestin second intronic enhancer that has previously been shown to drive transgene expression in CNS stem and progenitor cells.⁸⁸ *Rosa26-LSL-mPB-L3-ERT2* transgenic mice were obtained from Dr. Allan Bradley.⁸⁹ Lazy Piggy transgenic mice were produced by pronuclear microinjection into zygotes by the Transgenic Core at The Centre for Phenogenomics (TCP).⁹⁰ High-percentage male chimeras were crossed to C57/BL6 females. Germline transmission was confirmed by genotyping F1 offspring tail-clipped DNA. Primers used were: Lazy Piggy Fwd 5'-CGATAAAACACATGCGTC-3', Lazy Piggy Rev 5'-CTCCAAGCGGCGACTGAG-3'.

Lazy Piggy founder copy number was determined through qPCR as previously described.⁹¹ Briefly, a linear equation was modelled of C_T values against copy number from 9 known Lazy Piggy transposon plasmid standards in triplicate, then C_T values from triplicate founder samples were input to this model and resulting predicted copy numbers were averaged. Two founders (#129 and #137) were chosen for having “high” and “medium” Lazy Piggy copy numbers, respectively, on separate donor chromosomes to account for donor chromosome insertion bias.

Mouse studies

All procedures were performed in compliance with the Animals for Research Act of Ontario and the Guidelines of the Canadian Council on Animal Care. The Centre for Phenogenomics (TCP) Animal Care Committee reviewed and approved our protocol 19-0288H. In all cases, mice were maintained on a 12-hour light/dark cycle with free access to food and water. For all studies, mice of either sex were used, and randomly allocated to experimental groups. *Ptch1*^{+/-},²⁴ *Math1-Cre*,⁹² *Rosa26-LSL-SmoM2-YFP (SmoM2)*,⁹³ *Kcnb2*^{-/-} (*Kcnb2*^{tm1Lex}),⁹⁴ and *Nestin-Cre*⁹⁵ mice were previously described. All mice were bred and genotyped as recommended by Jackson Laboratories. *Math1-Cre*; *SmoM2* mice develop SHH MB due to expression of SmoM2—a constitutively active form of the SHH pathway receptor Smoothed—in cerebellar granule neuron precursors (CGNPs), achieved by CGNP-specific driver *Math1-Cre*.^{25,26} *Ptch1*^{+/-} mice develop SHH MB due to loss of one allele of the SHH pathway inhibitor *Ptch1*²⁴ and subsequent loss-of-heterozygosity, which drives constitutive SHH signaling in CGNPs.

For anti-Hedgehog therapy, 50 mg/kg vismodegib (GDC-0449, Selleck Chemical) was administered three times (P18, 19, 20) in 4.76% DMSO 0.5% methylcellulose 0.2% Tween 80 buffer by intraperitoneal injection. For single-dose BrdU labeling, mice were injected intraperitoneally with 50 mg/kg BrdU (Roche) in PBS. Tamoxifen-citrate mixture at 400 mg/kg was incorporated to the standard rodent diet premixed with ~5% sucrose as a palatability enhancer (Harlan Laboratories Teklad Diets). Tamoxifen chow was introduced once tumor-induced cranial bulge visualized, typically 45–60 days postnatal.

Mouse SOX2⁺ MB cell isolation and culture

Mouse SOX2⁺ MB cells were isolated as previously described.⁵⁵ Briefly, brain tumors from P7 *Math1-Cre*; *SmoM2* mice were dissociated by repetitive pipetting using ice-cold PBS without Mg²⁺ and Ca²⁺, followed by treatment using 50% Accutase (Stemcell Technologies) diluted in PBS. Dissociated cells were cultured on plates coated with poly-L-ornithine (Sigma-Aldrich) and laminin (Sigma-Aldrich), using Neurocult NS-A Basal media (StemCell Technologies) supplemented with 2 mM L-glutamine, N2, B27, 75 μg/ml BSA, 2 μg/ml Heparin, 10 ng/ml basic FGF and 10 ng/ml human EGF without addition of serum. All cell lines were regularly checked for mycoplasma infections.

For cell counting assays, cells were plated at a density of 2000 cells per well in poly-L-ornithine- and laminin-coated 12 well plates. At 2, 4, or 6 days after seeding, cells were resuspended using Accutase and incubated in isotonic solution. Cell count was acquired using a Multisizer 4 Coulter Counter (Beckman Coulter) using standard protocols and a threshold of 12 to 30 μm.

Human MB cell culture and experiments

To validate the selected hit genes, we performed gene knockdown in the ONS76 human MB cell line, cultured in DMEM supplemented with 10% fetal bovine serum and maintained at a constant temperature of 37 °C and a humidified atmosphere with 5% CO₂. siRNA (Thermo Scientific, #AM16708) and a GFP reporter were transfected using Lipofectamine 3000 (Invitrogen) according

to the manufacturer's instructions. Following 48 hours of transfection, gene expression was assessed using Real-time quantitative PCR (RT-qPCR) with specific primers. For RT-qPCR, total RNA was extracted from cells using the RNeasy Mini Kit (Qiagen) according to the manufacturer's instructions. RT-qPCR was performed using PowerUp SYBR Green Master Mix (Thermo Fisher Scientific, A25780) on a QuantStudio 5 Real-Time PCR System (Applied Biosystems). 18S rRNA was used as a housekeeping gene for the quantification of relative gene expression using $2^{-\Delta\Delta Ct}$.

The primers for RT-qPCR are:

KCNB1: 5'-CTGTCTGAAACCAGCTCAAG-3'; 5'-GTCTTCCAAGTCTGAACG-3'

KCNH2: 5'-CAACCTGGGCGACCAGATAG-3'; 5'-GGTGTGGGAGAGACGTTGC-3'

SMARCA4: 5'-AGTGCTGCTGTTCTGCCAAAT-3'; 5'-GGCTCGTTGAAGGTTTTTCAG-3'

DYNC1H1: 5'-GCCACCGTCAGTTTTGACAC-3'; 5'-AAATTGCCTCCACCAAACGC-3'

AHCYL: 5'-CCTGCGTAAAGGTGGTATGT-3'; 5'-GAGTGGAGGAAGGGCTATACTA-3'

METHOD DETAILS

Lazy Piggy plasmid construction

The Lazy Piggy transposon was custom synthesized and is shown in cartoon form in [Figure 1B](#). Mammalian-optimized PB minimum ITRs, as previously published,⁹⁶ were introduced to the T2/Onc2 SB transposon, nested between SB ITRs. T2/Onc2, as previously published,¹² contained a murine stem cell virus long terminal repeat (MSCV) 5' LTR, a splice donor (SD) from exon 1 of the mouse *Foxf2* gene, one splice acceptor (SA) from exon 2 of the mouse engrailed-2 (*En2*) gene and another from the carp β -actin gene, followed by a bidirectional SV40 poly(A) sequence. Restriction sites *AclI* and *ClaI* were introduced flanking the transposon sequence and a 4-copy concatemer was cloned into the pUC19 vector, hence termed "pLazyPiggy." Detailed cloning methods available upon request.

In vitro validation of the Lazy Piggy system

HEK293T cells were cultured in DMEM (GIBCO) supplemented with 10% fetal bovine serum at 37°C and 5% CO₂. 5×10^5 cells were seeded into each well of a 6-well plate 1 day prior to transfection. For each well, 2 μ g circular plasmids pCMV-HA-mPB-ERT2,⁹⁶ pLazyPiggy, and pCMV-SB11⁸ were transfected using Lipofectamine LTX as per manufacturer's protocol (Invitrogen). Cells were then incubated with 2 μ M 4-hydroxytamoxifen (4-OHT) for 24 hours. Cells were then collected and gDNA were extracted for PCR excision assays. Primers for amplifying Lazy Piggy-transposon mobilization were based on the cloning vector sequences adjacent to the inverted repeats/direct repeats (left) (IRDRL) and inverted repeats/direct repeats (right) (IRDRR) of the Lazy Piggy transposon, 5'-CGTT CACGACGTTGTAAAACGACG-3' and 5'-CGATAATTAACCCTCACTAAAGGG-3', respectively. The input represents genomic DNA with Lazy Piggy intact transposon (2791bp), post-SB mobilization (166bp) and post-PB re-mobilization (681bp) in the presence of 4-OHT. Detailed PCR protocol methods are available upon request.

Western blot analysis

Western blot analysis was performed on postnatal day 30 cerebellum from transgenic mice *R26:LSL-PB-ERT2^{+/-}* mice crossed with *Nestin-Cre^{+/-}* mice. For Western blot of human ONS76 MB cells, the cells were seeded in 6-well plates and grown to 70-80% confluence. Lipofectamine 3000 (Thermo Fisher Scientific) was used for transfection according to the manufacturer's instructions. Cells were transfected with either pcDNA 6.2 N-emGFP vector (Invitrogen) or pcDNA 6.2 N-emGFP and *KCNB2* plasmid. Extracted protein was run on Novex Wedgewell 8-16% Tris-Glycine gradient gels (Thermo Fisher) then transferred to PVDF membranes. Membranes were then blocked in TTBS with 5% Skim milk (Bioshop #SKI400) for two hours and probed overnight in TTBS/1% skim milk with a 1:3000 dilution of mouse anti- α -Tubulin (Sigma Aldrich #T6199), or a 1:500 dilution of mouse anti-ER α antibody (SCBT sc-56833). Membranes were then washed in TTBS/1% skim milk, incubated with secondary antibodies (1:5000 anti-mouse IgG, HRP-linked antibody (Cell Signaling #7076S)). Finally, blots were washed in TTBS/1% skim milk, incubated in Pierce ECL Western substrate (Thermo Fisher #32209) and signal visualized on a Bio-Rad ChemiDoc system.

Necropsy, tumor collection, and histological analysis

Experimental mice were monitored for tumor formation over a period of 365 days. When mice reached humane endpoint, they were sacrificed according to Canadian Council on Animal Care (CACC) guidelines. Upon sacrifice, cerebellar tumors were collected and divided into smaller pieces and frozen on dry ice. Samples were placed at -80 °C for long-term storage or in RNAlater (Sigma). Formalin-fixed tissue samples were paraffin-embedded by the Pathology Core at the Centre for Modeling Human Disease (CMHD) in TCP. 5 μ m sections were stained with Hematoxylin and Eosin and used for histological analysis.

Histological analysis

Formalin-fixed tissue samples were paraffin-embedded by the Pathology Core at the Centre for Modeling Human Disease (CMHD) in TCP. 5 μ m sections were stained with Hematoxylin and Eosin, and used for histological analysis.

Library preparation and sequencing

Restriction-splink PCR was performed based on previous protocols.^{97,98} In brief, mouse tumor gDNA was extracted and mechanically sheared to 300 bp fragments using a Covaris S220 sonicator. End repair was then performed using an EpiCentre End-It Kit,

followed by adaptor ligation. With splinkerette-adaptors ligated at both ends, BamHI was used to digest and remove gDNA fragments. Primary and secondary PCR amplifications were performed using primers listed below for Left & Right amplification and for barcoding, respectively. Finally, purified PCR products were sent for 454 parallel sequencing at the Ontario Institute for Cancer Research. Genomic DNA libraries from Lazy Piggy tumors were prepared as sequenced as previously described.⁹⁹ Three libraries were prepared to identify different types of Lazy Piggy insertion events. To identify all Lazy Piggy insertions, Lazy Piggy insertions that had undergone PB excision, and Lazy Piggy insertions that had not undergone PB excision, the IR, PB, and JX libraries were prepared using primers corresponding to individual SB ITRs, both SB ITRs, and SB plus PB ITRs, respectively.

Lazy Piggy read processing, alignment and analysis

Processing and gCIS analysis of Lazy Piggy transposon insertion sites were performed using a custom R script. To correct for technical alignment jitter in insertion mapping, insertions were grouped by sample and orientation (left or right), then counts were aggregated for insertions within 5bp of each other. We removed insertions mapping to non-standard or donor chromosomes, those with single read support, or those detected in *Ptch1*^{+/-} control mice. A dynamic filter was used to categorize insertions as clonal or subclonal, as previously described.^{32,99} For each library, three thresholds were calculated using the insertion data: (i) >95th percentile of reads under the negative binomial distribution fit to the number of sites with 1–3 reads, (ii) 1% of the read count of the most abundant insertion site, (iii) 0.1% of the total read number. The most stringent value was the threshold for clonal insertions and the second-most was the threshold for the clonal/subclonal category. Gene-centric common insertion site (gCIS) analysis was performed using clonal/subclonal insertions. gCIS genes were RefSeq genes (+15kb buffer) with insertions in at least 3 separate tumors and Bonferroni-corrected p value <0.05 from a Chi-square test of observed and expected insertion counts given the number of TA dinucleotide sites within the gene relative to the whole genome and the total number of insertions within each tumor. Known false positive genes *En2*, *Sfi1*, and *Foxf2* were removed since they contain sequence homology with the Lazy Piggy transposon. To identify tumor maintenance genes, we compared gCIS genes from PB libraries in mice with and without tamoxifen treatment. To assess robustness of tamoxifen-induced PB remobilization, Jaccard similarity scores were calculated for all pair-wise library comparisons in IR and JX libraries. The complete raw insertion data including genomic coordinates, library type, and read depth are reported in the GitHub repository.

Bulk RNA-seq library preparation, data preprocessing, and analysis (Lazy Piggy tumors)

Bulk RNA-seq libraries were prepared and sequenced as previously described¹⁰⁰ using the Miseq system with 5 samples pooled per lane and mean 50 million reads per sample. After raw FASTQ quality check with FastQC, reads were aligned using STAR (2.5.4b) to mouse genome mm9 using the annotation file *Mus musculus* NCBIM37v67 (downloaded from Ensembl) with masking for the *En2* gene, whose splice acceptor sequence is contained in the Lazy Piggy transposon.¹⁰¹ The “ReadsPerGene” raw counts from STAR were used for differential expression analysis with DESeq2 (1.34.0) using genes with non-zero counts in at least two samples per tamoxifen treatment group.¹⁰² Dimensionality reduction by UMAP¹⁰³ was then performed to visualize the distribution of tamoxifen receipt status across clusters following variance-stabilizing transformation of raw counts in DESeq2.

Bulk RNA-seq analysis (human MB and normal cerebellum)

Normalized counts were generated from published human MB and normal cerebellar bulk RNA-seq data as described previously.^{34–37} DESeq2 (1.34.0) was used for differential expression analysis.¹⁰²

Single cell RNA-seq analysis

Normalized counts for human SHH MB samples were downloaded from GEO⁵² and UCSC Cell Browser⁵³ and prepared as Seurat (4.1.0) objects. UMAP embeddings for the data from Riemondy et al. were directly downloaded. UMAP embeddings for Hovestadt et al. were calculated following the Seurat SCTransform() vignette and batch effects corrected using harmony (0.1.0) with all default settings.

Immunocytochemistry

Immunocytochemistry was performed on cultured cells as previously described.¹⁰⁴ Briefly, cells on glass coverslips were fixed for 15 minutes with 4% PFA and then permeabilized with 0.1% Triton X-100 in PBS (PBST). Cells were subsequently blocked with 10% normal goat or horse serum in PBST for one hour at room temperature and incubated with primary antibodies in blocking solution overnight at 4° C, followed by incubation with fluorophore-conjugated secondary antibodies (1:400–1000) and 1 μg/ml DAPI (Sigma-Aldrich) for one hour at room temperature. For F-actin staining, cells were stained with 1:500 Alexa Fluor 488 Phalloidin (Invitrogen). Coverslips were mounted onto glass slides using Prolong Gold (Invitrogen). The primary antibodies include: chicken anti-GFP (Antibodies Incorporated #GFP-1020, 1:1000), mouse anti- α -Tubulin (Sigma-Aldrich #T6199, 1:1000), mouse anti-BrdU (DSHB #G3G4, 1:1000), mouse anti-Caveolin-1 (Novus #NB100-615, 1:200), rabbit anti-Caveolin-1 (Cell Signaling Technology #3267, 1:400), rabbit anti-Clathrin Heavy Chain (Cell Signaling Technology #4796, 1:100), rabbit anti-pEGFR (Cell Signaling Technology #3777, 1:800), rabbit anti-pEGFR (abcam #ab40815, 1:250), rabbit anti-pERM (Cell Signaling Technology #3726, 1:200), rabbit anti-Rab5 (Cell Signaling Technology #3547, 1:400), and rat anti-Ki67 primary antibody (Invitrogen 14-5698-82, 1:500). Images were acquired using a Leica SP8 Lightning Confocal DMI6000 microscope. Images were analyzed using Imaris software.

Tissue preparation and immunohistochemistry

Postnatal (P7 and P21) mice were transcardially perfused with ice-cold PBS, followed by 4% PFA. Brains were removed and fixed in 4% PFA overnight upon collection. Brains were then cryopreserved in 30% sucrose for 48–72 hours, mounted in O.C.T. compound (Tissue-tek), and cryo-sectioned at 10–12 μm . For immunohistochemistry, frozen sections were dried at room temperature for 30 minutes and rehydrated in PBS with 0.1% Tween (PBSTw). Antigen retrieval was performed in 10mM citrate buffer, pH 6.0, for 20 minutes at 95° C. Sections were blocked with 10% normal goat serum in PBSTw for one hour at room temperature and incubated with primary antibodies in blocking solution overnight at 4° C, followed by incubation with fluorophore-conjugated secondary antibodies (1:200–500) and 1 $\mu\text{g}/\text{ml}$ DAPI (Sigma-Aldrich) for one hour at room temperature. Sections were then mounted with glass coverslips using Aquamount (Fisher Scientific). The primary antibodies include: mouse anti-BrdU (DSHB #G3G4, 1:100), rat anti-BrdU (abcam #6326, 1:500), mouse anti-KCNB2 (NeuroMab #75-369, 1:100), mouse anti-PCNA (Santa Cruz Biotechnology #sc-56, 1:200), mouse anti-SOX2 (abcam #ab79351, 1:100), rabbit anti-SOX2 (abcam #ab97959, 1:200), rabbit anti-Caveolin-1 (Cell Signaling Technology #3267, 1:200), rabbit anti-DCX (abcam #ab18723, 1:200), rabbit anti-Ki67 (abcam #ab15580 1:200), rat anti-Ki67 (Ebioscience #14-5698-82, 1:200), rabbit anti-NeuN (abcam #ab104225, 1:200), rabbit anti-pEGFR (abcam #ab40815, 1:250), rabbit anti-pERK1/2 (Cell Signaling Technology #4370, 1:200), rabbit anti-pERM (Cell Signaling Technology #3726, 1:200). Cell death was determined using TUNEL (Cat. # S7110, Sigma-Aldrich) according to the manufacturer's instructions. Images were acquired using a Leica SP8 confocal microscope or a Quorum spinning disc confocal microscope. Images were analyzed using Imaris software. Hematoxylin and eosin staining was performed on paraffin-embedded sections and imaged using a 3D Histech Panoramic 250 Flash II Slide Scanner.

In vitro limiting dilution assay

Cells were plated in serial dilutions on non-adherent 96-well plates and in six biological replicates under stem cell conditions. Serial dilutions ranged from 2000 cells to 3 cells per well. After 7 days of plating, each well was scored for negative spheres. Data was plotted and tested for inequality in frequency between multiple groups and tested for adequacy of the single-hit model using Extreme Limiting Dilution Analysis (ELDA) software.

Atomic force microscopy

Force-displacement data were collected at room temperature using atomic force microscopy (AFM, Bioscope Catalyst, Santa Barbara, CA) mounted on an inverted microscope (Nikon Eclipse Ti2). Force-displacement-speed data were measured at the cell center. Measurement of cells in each petri dish was completed within 20 mins after being taken out of the incubator. The AFM probe with a spherical tip was used to measure the cell stiffness, using the Hertz model to calculate the cell stiffness value from the force-displacement data. The AFM probe with a needle shape tip was used to indent and penetrate the cell membrane, for measuring the cell membrane tension. The cell membrane tension results were calculated based on the force-displacement data before the membrane rupture was observed (larger than 100 pN) and using the mechanics model based on previous studies.¹⁰⁵ The AFM probes used for cell stiffness measurement experiments were biosphere B100-CONT (Nanoandmore, USA), with a nominal spring constant of 0.2 N/m. The AFM probes used for cell membrane tension experiments were Focused-Ion-Beam modified probe MSNL-10 (Bruker, USA), with a nominal spring constant of 0.03 N/m.¹⁰⁶ The spring constant of each probe was calibrated using thermal spectroscopy (Nanoscope 8.10). The loading speeds were set to be 10 $\mu\text{m}/\text{s}$ to minimize the effects from the viscoelastic properties of the cell. Data analysis for quantifying cell stiffness and cell membrane tension was conducted in MATLAB. The code of data analysis for rejecting the non-rupture case is available for download at https://github.com/XianShawn/Nuclear_Mechanics.

For AFM measurements after hypoosmotic shock the experiments were performed on MPCs collected at postnatal day 7. The cells were cultured on PLO and laminin-coated glass coverslips. For chronic hypotonic shock, the cells were exposed to the hypotonic solution for 1 week, with the medium changed every 3–4 days. The isotonic solution consisted of mNSA medium with an osmolarity of 360 mOsm. The hypotonic solution was prepared by supplementing the mNSA medium with 30% de-ionized water, resulting in an osmolarity of 250 mOsm.

Micropipette aspiration

The micropipette was fabricated from a glass capillary using a commercialized micropipette puller system (Model P-97, Sutter Instrument). The inner diameter of the micropipette tip is 2 μm . To make the tip horizontal under the microscope for clear aspiration observation, the tip was bent by 45° using a Microforge (Model MF-1, TPI Instruments). The pressure applied to the tip of the micropipette was controlled by a pneumatic microinjection pump (Digital Microinjector from Sutter Instrument). Before aspiration, a positive pressure was applied to the micropipette tip to balance the capillary force. During aspiration, the micropipette tip was gently brought into contact with the cell surface and the pressure applied to the tip was reduced by a set amount. The entire aspiration process was recorded by a camera (scA1300-32gm, Basler) at 33 frames per second. The aspiration length and speed of the cell inside the micropipette was measured manually. The inner cell pressure was calculated using the standard linear solid model.

Electrophysiology

Cells were cultured on laminin-coated plastic coverslips for 48–72 hours. Coverslips were transferred to a recording chamber filled with bath solution. The bath solution consisted of (in mM) 118 NaCl, 3 KCl, 2.5 CaCl₂, 1.5 MgCl₂, 10 glucose, and 10 HEPES (pH adjusted to 7.4 with NaOH). Patch pipettes (borosilicate glass) for recording, with resistance of around 4 M Ω , were filled with intracellular solution consisting of 125 mM KCl, 11 mM EGTA, 1 mM CaCl₂, 1.5 mM MgCl₂, and 10 mM HEPES (pH adjusted to 7.2 with KOH). Whole-cell currents were recorded using an Axopatch 700B amplifier (Molecular Devices). All experiments were performed at

room temperature. Pipette and whole cell capacitance were compensated. The voltage protocol consisted of 200 ms pulses from -80 mV to +80 mV (20 mV voltage steps). Data were acquired online, filtered at 4 kHz, digitized at 10 kHz, and analyzed offline using pClamp10 (Molecular Devices). Leak currents before voltage stimulations were subtracted off-line. I-V curves were generated by plotting peak current amplitude at different voltages. Data were quantified and graphed using GraphPad Prism.

QUANTIFICATION AND STATISTICAL ANALYSIS

No statistical methods were used to pre-determine sample sizes. The statistical analyses were performed after data collection without interim data analysis. No data points were excluded. Two-tailed Student's t-test was performed for comparison between two groups of samples. Two-Way ANOVA analyses were used to assess significance of multiple data points. The Kaplan–Meier estimator was used to generate survival curves using the R package {survival}.¹⁰⁷ Differences between survival curves were calculated using a log-rank test. All data were collected and processed randomly. All data are expressed as mean \pm SEM. We considered a *P* value less than 0.05 to be statistically significant.

Supplemental information

**A forward genetic screen identifies potassium
channel essentiality in SHH
medulloblastoma maintenance**

Jerry J. Fan, Anders W. Erickson, Julia Carrillo-Garcia, Xin Wang, Patryk Skowron, Xian Wang, Xin Chen, Guanqiao Shan, Wenkun Dou, Shahrzad Bahrampour, Yi Xiong, Weifan Dong, Namal Abeysundara, Michelle A. Francisco, Ronwell J. Pusong, Wei Wang, Miranda Li, Elliot Ying, Raúl A. Suárez, Hamza Farooq, Borja L. Holgado, Xiaochong Wu, Craig Daniels, Adam J. Dupuy, Juan Cadiñanos, Allan Bradley, Anindya Bagchi, Branden S. Moriarity, David A. Largaespada, A. Sorana Morrissy, Vijay Ramaswamy, Stephen C. Mack, Livia Garzia, Peter B. Dirks, Xuejun Li, Siyi Wanggou, Sean Egan, Yu Sun, Michael D. Taylor, and Xi Huang

Supplemental Figure 1. Establishing Lazy Piggy transposition *in vitro* and *in vivo*, related to Figure 1

(A) PCR amplification of the Lazy Piggy concatemer region in transfected 293T cells. Combinations performed in triplicate with 50ng, 100ng, and 150ng input DNA each. Transposon mobilization scars are seen with piggyBac transposase (PB) and tamoxifen administration (left) and with Sleeping Beauty (SB) transposase (right).

(B) Immunofluorescence of 293T cells transfected with the Lazy Piggy transposon and piggyBac-ER transposase demonstrated nuclear localization of the PB transposase following tamoxifen administration.

(C) Microinjection of 4-unit concatemer of the Lazy Piggy transposon generated 7 founder mice.

(D) qPCR determination of Lazy Piggy concatemer copy number in founder mice.

(E) Western blot analysis of cerebellar ER α expression in *R26-LSL-PB-ER^{T2+/-}* mice when crossed with *Nestin-Cre^{+/-}* mice. Expression of ER α is seen only when both transgenes present, indicating successful Cre-mediated recombination.

(F) PCR amplification of the Lazy Piggy concatemer region demonstrates SB mobilization and PB mobilization with tamoxifen treatment in *Ptch1^{+/-}*; *Nestin:Luc-SB100^{+/-}*; *Lazy Piggy^{+/-}*; *Nestin-Cre^{+/-}*; *R26-LSL-PB-ER^{T2+/-}* mice. Combinations performed in triplicate with 50ng, 100ng, and 150ng input DNA each.

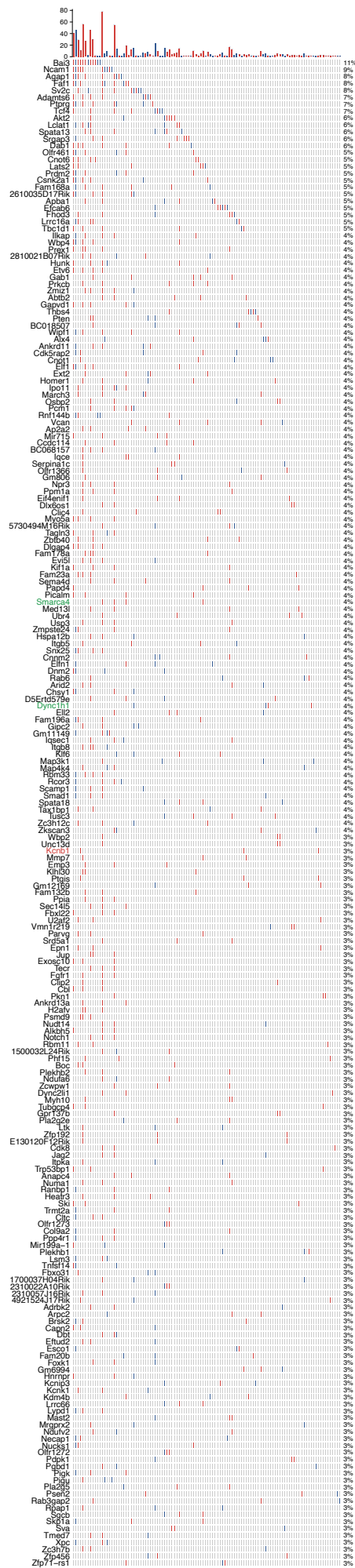
(G) Tumors in *Ptch1^{+/-}*; *Nestin:Luc-SB100^{+/-}*; *Lazy Piggy^{+/-}*; *Nestin-Cre^{+/-}*; *R26-LSL-PB-ER^{T2+/-}* mice histologically resemble human MB (H&E staining).

(H-I) Representative bioluminescent imaging (BLI) of Lazy Piggy mice. Time-course BLI of two representative animals with full quintuple genotype **(H)** and quadruple mice lacking the *Nestin-Luc-SB100* allele **(I)**. Note, radiance scale bars are conserved within sample but differ between samples.

(J) Mouse identification, date-of-birth, and duration of treatment in tamoxifen-treated tumors used for bulk RNA sequencing.

(K) Tamoxifen treatment was not associated with overall survival in *Ptch1^{+/-}*; *Nestin:Luc-SB100^{+/-}*; *Lazy Piggy^{+/-}*; *Nestin-Cre^{+/-}*; *R26-LSL-PB-ER^{T2+/-}* mice.

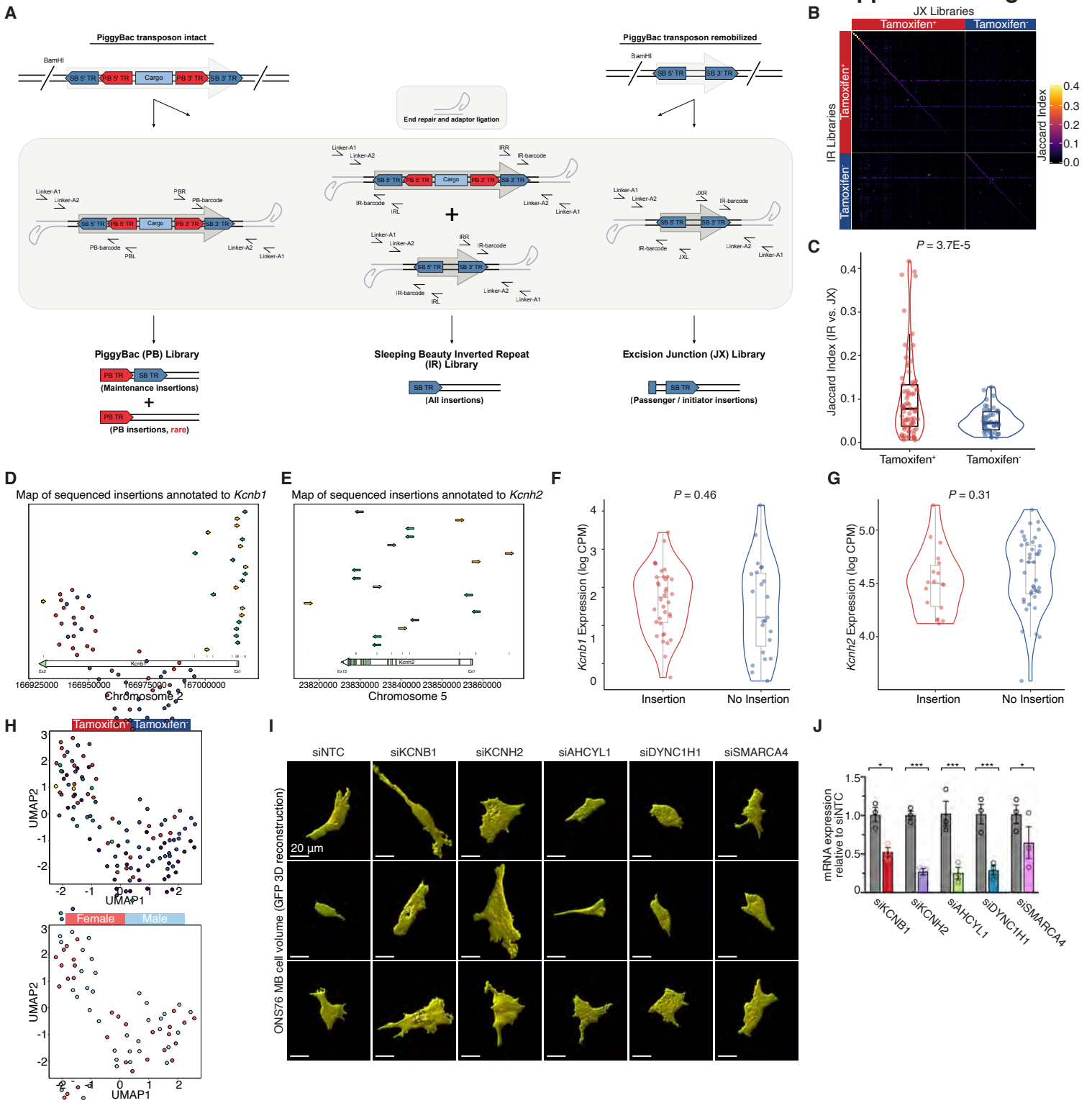
(L-M) Kaplan-Meier survival analysis of *Ptch1^{+/-}*; *Nestin-Cre^{+/-}*; *LazyPiggy^{+/-}*; *R26-LSL-PB^{ERT2+/-}* mice with Lazy Piggy concatemers from two different donor chromosomes, stratified by tamoxifen treatment status.



Supplemental Figure 2. Oncoprint of SB-induced gCIS insertions reflecting the baseline insertional landscape of primary SB-mediated remobilization, related to Figure 1

Red and blue bars indicate SB gCIS insertions in tamoxifen-treated and -untreated tumors, respectively.

Supplemental Figure 3



Supplemental Figure 3. Library preparation, analysis, and functional validation of Lazy Piggy transposon remobilization in MB, related to Figure 2

(A) Cartoon illustrating library preparation workflows for Sleeping Beauty Inverted Repeat (IR), piggyBac (PB), and Excision Junction (JX) libraries.

(B-C) Heatmap **(B)** and quantification **(C)** of Jaccard score similarity matrix for clonal IR and JX library insertions in sequenced mouse tumors, showing an expected higher proportion of IR/JX overlap in tamoxifen-treated versus -untreated tumors.

(D) Map of all sequenced insertions annotated to *Kcnc1* suggests gain-of-function given biases toward intronic, 5', and sense-oriented insertions. Green and yellow arrows indicate sense and anti-sense insertions, respectively.

(E) Map of all sequenced insertions annotated to *Kcnc2* suggests loss-of-function given the span of insertions across the entire coding sequence of *Kcnc2* which would yield a truncated and non-functional channel. Red and blue coloring indicate orientation of insertions.

(F-G) Log CPM-normalized RNA-seq values for *Kcnc1* **(F)** and *Kcnc2* **(G)** expression, stratified by the presence or absence of Lazy Piggy insertions annotated to each respective gene.

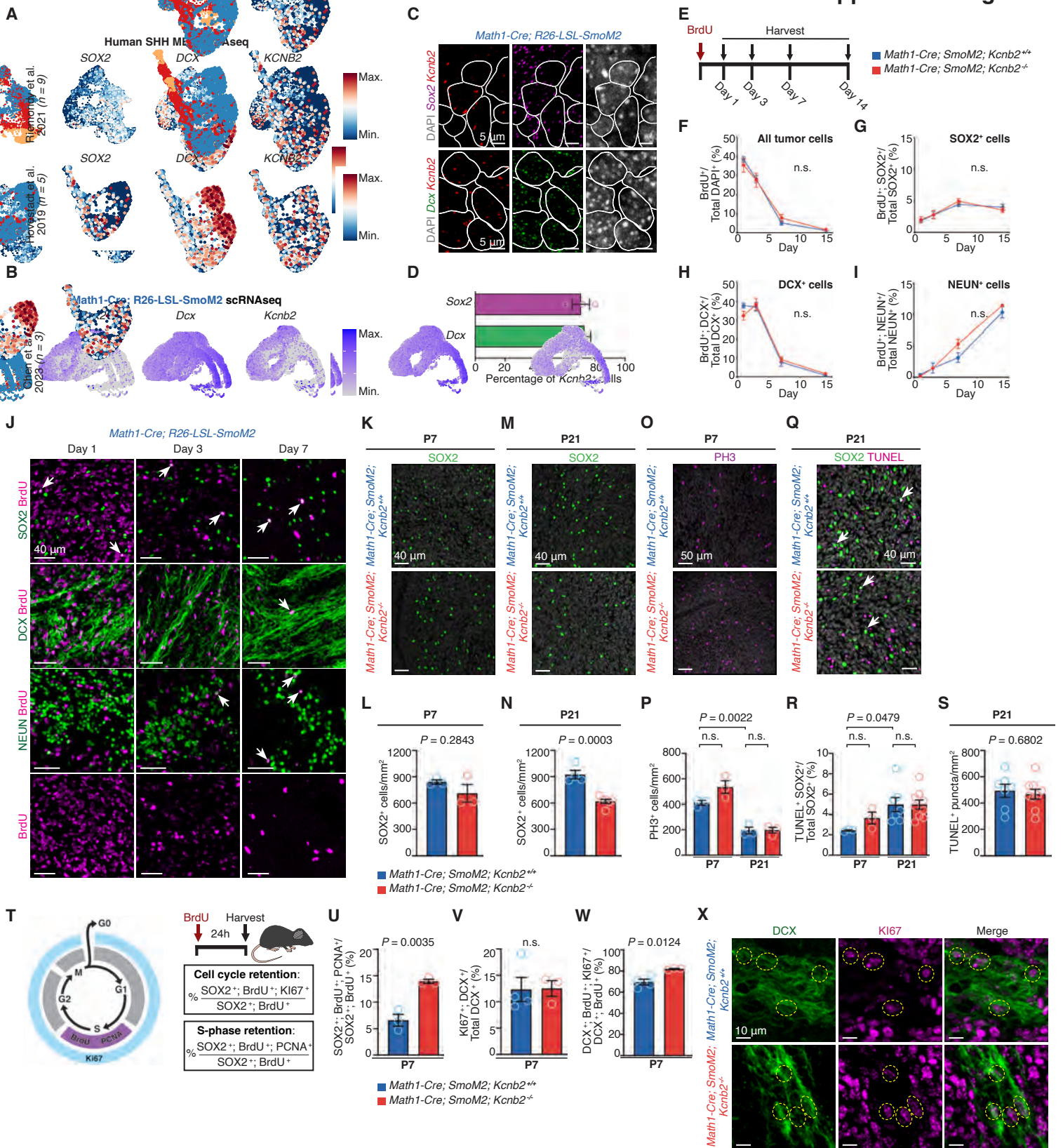
(H) Dimensionality reduction by uniform manifold approximation and projection (UMAP) of DESeq2-normalized RNA-seq counts from tamoxifen-treated and untreated tumors.

(I) Representative images of ONS76 GFP 3D reconstruction to demonstrate cell volume changes induced by siRNA-mediated knockdown of candidate genes.

(J) Assessment of knockdown efficiency by qPCR upon treatment with siRNA targeting of the indicated genes.

Supplemental Figure 4. Assessment of KCNB2 expression and function in normal physiology and development, related to Figure 3

- (A) Survival of *Kcnc2*^{+/+}, *Kcnc2*^{+/-}, and *Kcnc2*^{-/-} mice. *Kcnc2* is not necessary for murine development, function.
- (B) Expected Mendelian offspring genotype distribution from crossing *Kcnc2*^{+/-} parents indicates lack of embryonic lethality with knockout.
- (C) Weight of *Kcnc2*^{+/+}, *Kcnc2*^{+/-}, and *Kcnc2*^{-/-} mice at postnatal day 21 shows no differences across genotypes.
- (D) Litter sizes from breeding pairs of *Kcnc2*^{+/+}, *Kcnc2*^{+/-}, and *Kcnc2*^{-/-} mice. *Kcnc2* is not necessary for fertility.
- (E) Representative images P21 *Kcnc2*^{+/+}, *Kcnc2*^{+/-}, and *Kcnc2*^{-/-} littermate mice, which do not display gross morphological differences.
- (F) Representative images of P7 and P30 brains of *Kcnc2*^{+/+} and *Kcnc2*^{-/-} mice, which do not display gross morphological differences.
- (G) Representative histology of sagittal brain sections from P7 and P30 mice indicates no gross morphological differences in the absence of *Kcnc2*.
- (H) Representative immunohistochemistry images from cerebella of P7 *Kcnc2*^{+/+} and *Kcnc2*^{-/-} mice, which do not display differences in distribution or intensity.
- (I) Representative immunohistochemistry images from cerebella of P30 *Kcnc2*^{+/+} and *Kcnc2*^{-/-} mice, which do not display differences in distribution or intensity.
- (J) Quantification of molecular layer, internal granule layer, external granule layer thickness, Calbindin⁺ Purkinje neuron and SOX2⁺ Bergmann glia populations of P7 *Kcnc2*^{+/+} and *Kcnc2*^{-/-} mice, which do not display quantitative differences.
- (K) Quantification of molecular layer, internal granule layer thickness, Calbindin⁺ Purkinje neuron and SOX2⁺ Bergmann glia populations of P30 *Kcnc2*^{+/+} and *Kcnc2*^{-/-} mice, which do not display quantitative differences.
- (L) GTEx analysis of *KCNB2* expression across non-tumor human tissues.



Supplemental Figure 5. KCNB2 transcriptomic analysis in MB and assessment of KCNB2 function in the SHH MB cellular hierarchy, related to Figure 3

(A-B) *KCNB2/Kcnb2* expression is observed in both human and mouse *SOX2/Sox2*⁺ and *DCX/Dcx*⁺ MB cells in previously published human (A) and mouse (B) SHH MB scRNA-seq.

(C-D) Single-molecule fluorescence *in situ* hybridization (RNAscope) analysis of *Kcnb2*, *Sox2*, and *Dcx* transcripts from mouse SHH MB. Representative images containing lines comprised of dashed lines in **(C)** demarcate nuclear boundaries, and quantification of *Kcnb2*⁺ cells co-expressing either *Sox2* or *Dcx* transcripts **(D)**. Stem and mitotic progenitor cells express *Kcnb2* within the SHH MB hierarchy.

(E) Experimental design of BrdU label retention analysis. *Math1-Cre; SmoM2; Kcnb1^{+/+}* and *Math1-Cre; SmoM2; Kcnb2^{-/-}* mice were injected with a single dose of BrdU and sacrificed at the indicated timepoints (*n* = 3-4 mice per group).

(F-I) Percentage of BrdU retention in all tumor cells **(F)**, *SOX2*⁺ cells **(G)**, *DCX*⁺ cells **(H)**, and *NEUN*⁺ cells **(I)**. Label retention dynamics are not perturbed with *Kcnb2* loss of function, suggesting knockout does not skew progression from the normal SHH MB cellular hierarchy.

(J) Representative images of BrdU label retention in *SOX2*⁺, *DCX*⁺, and *NEUN*⁺ cells at 1, 3, and 7 days after BrdU injection in MB of *Math1-Cre; SmoM2* mice.

(K-N) Quantification of *SOX2*⁺ cells in SHH MB from *Math1-Cre; SmoM2; Kcnb2^{+/+}* and *Math1-Cre; SmoM2; Kcnb2^{-/-}* mice shows reduced abundance of SHH MB stem cells with *Kcnb2* loss of function at P21 but not P7.

(O-P) Quantification of Phospho-Histone 3⁺ (*PH3*⁺) cells in SHH MB from *Math1-Cre; SmoM2; Kcnb2^{+/+}* and *Math1-Cre; SmoM2; Kcnb2^{-/-}* mice indicates no change in overall mitotic index with *Kcnb2* loss of function, but decrease from P7 to P21.

(Q-S) Quantification and representative immunohistochemistry of *TUNEL*⁺ puncta and *SOX2*⁺ cells in SHH MB of P7 and P21 *Math1-Cre; SmoM2; Kcnb2^{+/+}* and *Math1-Cre; SmoM2; Kcnb2^{-/-}* mice indicates no change in apoptotic rate with *Kcnb2* loss of function, but increase from P7 to P21.

(T) Schematic of BrdU pulse experiment.

(U) Quantification of *SOX2*⁺ S-phase retention at P7 reveals loss of *Kcnb2* function is specifically associated with cell cycle retention at S-phase.

(V-X) Representative immunohistochemistry and quantification of *DCX* and *Ki67* from P7 MBs indicates *Kcnb2* loss of function does not significantly alter proliferation of transit-amplifying *DCX*⁺ progenitor cells. **(W)** Quantification of *DCX*⁺ cell cycle retention at P7. Loss of *Kcnb2* function is associated with a mild cell cycle retention phenotype in *DCX*⁺ cells.

Supplemental Figure 6. Characterization of protein and RTK changes upon KCNB2 depletion in SOX2⁺ MPCs *in vitro*, related to Figure 5

(A) Western blot and quantification of 4 pairs of *Math1-Cre; SmoM2; Kcnb2^{+/+}* and *Math1-Cre; SmoM2; Kcnb2^{-/-}* MPCs for pEGFR, EGFR, pERM, Ezrin, and Coomassie blue dye. All quantifications were normalized to the total Coomassie blue signal per lane. Loss of *Kcnb2* function is associated with decreased pEGFR and membrane tether pERM.

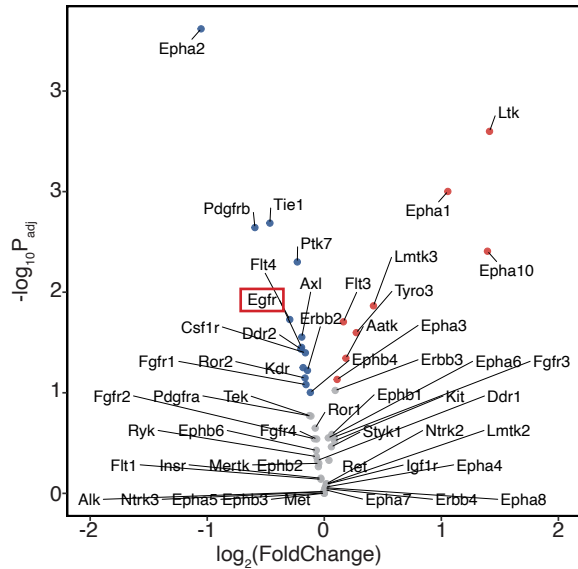
(B) Western blots in (A) with lane markers included.

(C) SOX2⁺ MPCs were cultured in media with indicated concentrations of EGF and bFGF and assessed for relative viability by MTS assay (left) and crystal violet staining (right). Viability is more crucially dependent on EGF than FGF.

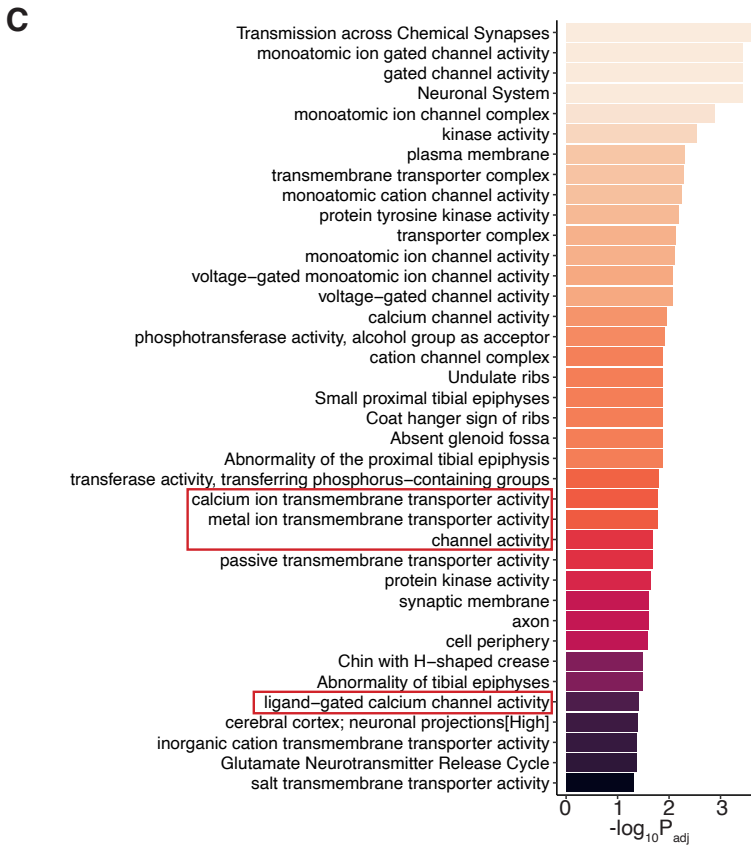
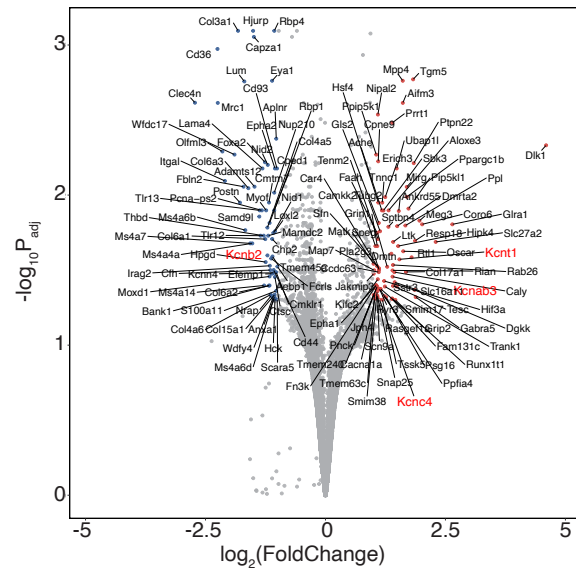
(D) Phospho-RTK array of SOX2⁺ MPCs from *Math1-Cre; SmoM2; Kcnb2^{+/+}* and *Math1-Cre; SmoM2; Kcnb2^{-/-}* mice. Each array was performed on a separate biological replicate. Loss of *Kcnb2* function is associated with diminished EGFR signal.

(E) Phospho-RTK array legend and map.

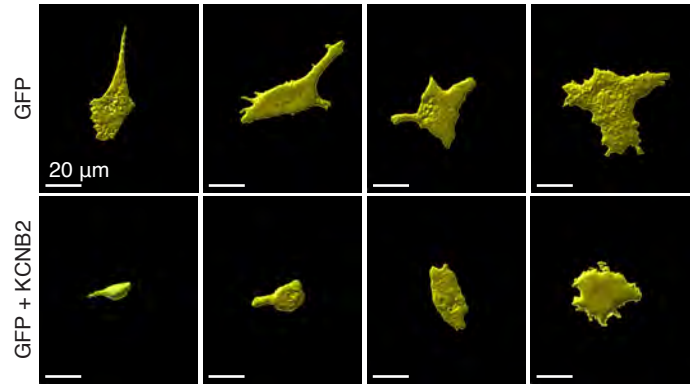
A *Math1-Cre; SmoM2; Kcnb2^{+/+}* vs *Math1-Cre; SmoM2; Kcnb2^{-/-}*



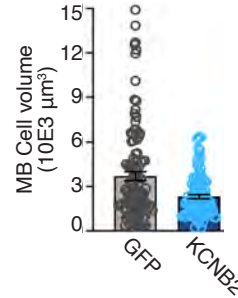
B *Math1-Cre; SmoM2; Kcnb2^{+/+}* vs *Math1-Cre; SmoM2; Kcnb2^{-/-}*



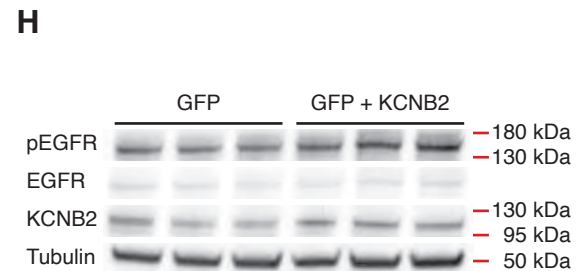
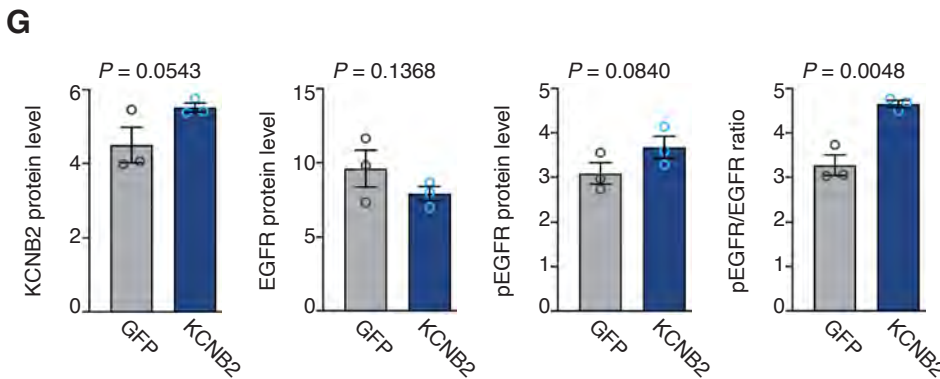
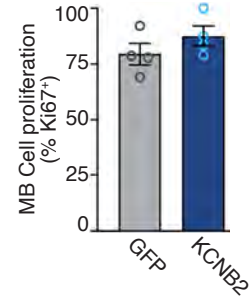
D ONS76 MB cell volume (GFP 3D reconstruction)



E $P = 0.0056$



F $P = 0.0349$



Supplemental Figure 7. Bulk RNA-seq of *Math1-Cre; SmoM2; Kcnb2^{+/+}* and *Math1-Cre; SmoM2; Kcnb2^{-/-}* P21 tumors and KCNB2 overexpression experiments in human MB cells *in vitro*, related to Figure 6

(A) DESeq2 differential expression analysis of $n=3$ *Kcnb2* knockout tumors and $n = 7$ control tumors reveals downregulation of EGFR following *Kcnb2* knockout.

(B) DESeq2 differential expression analysis of $n=3$ *Kcnb2* knockout tumors and $n = 7$ control tumors reveals compensatory upregulation of potassium channels following *Kcnb2* knockout.

(C) gProfiler2 pathway enrichment of significantly upregulated genes in *Kcnb2* knockout tumors compared to controls reveals enrichment for various ion channel terms.

(D) Representative 3D reconstructions of GFP⁺ volume in ONS76 MB cells upon transfection with GFP alone and GFP + KCNB2.

(E) Quantification of ONS76 MB cell volume upon transfection with GFP alone and GFP + KCNB2. KCNB2 over-expression drives potassium efflux to reduce cell volume.

(F) Quantification of ONS76 MB cell proliferation upon transfection with GFP alone and GFP + KCNB2. KCNB2 over-expression increases Ki67 positivity of MB cells.

(G-H) Quantification of protein levels of KCNB2 and EGFR signaling upon KCNB2 over-expression in ONS76 MB cells. KCNB2 over-expression increases KCNB2 protein levels, and increases EGFR phosphorylation.